Accepted Manuscript

Geological Society, London, Special Publications

Petrogenesis and Ni-Cu-(PGE) prospectivity of the Mount Ayliff Complex in the Karoo Igneous Province: new insights from the Ingeli and Horseshoe lobes

W. D. Smith, B. Albrechtsen, W. D. Maier & J. E. Mungall

DOI: https://doi.org/10.1144/SP552-2023-35

To access the most recent version of this article, please click the DOI URL in the line above. When citing this article please include the above DOI.

Received 11 February 2023
Revised 31 August 2023
Accepted 11 September 2023

Supplementary material at https://doi.org/10.6084/m9.figshare.26207275

Petrogenesis and Ni-Cu-(PGE) prospectivity of the Mount Ayliff Complex in the Karoo Igneous Province: new insights from the Ingeli and Horseshoe lobes

W. D. Smith[1]*, B. Albrechtsen[2], W. D. Maier[3], & J. E. Mungall[1]

[1]Department of Earth Sciences, Carleton University, 1125 Colonel By Drive, Ottawa, ON K1S 5B6, Canada

[2]University of Arizona Arthritis Center, 1501 N. Campbell Avenue, Tucson, Arizona, United States

[3]School of Earth and Environmental Sciences, Cardiff, University, Cardiff, CF10 3AT, United Kingdom

*Corresponding author: williamsmith3@cunet.carleton.ca (ORCID = 0000-0002-6523-7864)

Abstract

The Mount Ayliff Complex comprises five cognate mafic-ultramafic bodies emplaced along the southern margin of the Kaapvaal Craton. This study examines the Ingeli and Horseshoe lobes and assesses their magmatic sulphide prospectivity with respect to the Insizwa lobe, which hosts massive sulphides at its Waterfall Gorge occurrence. Ingeli consists of 465 m of olivine-chromite cumulates overlain by 340 m of (olivine-)gabbronorite, while Horseshoe consists of 45 m of olivine gabbronorite overlain by 5 m of gabbro. Ingeli possesses sparsely disseminated sulphides at its mafic-ultramafic transition, whereas disseminated sulphides are present throughout Horseshoe. A petrogenetic model is proposed, whereby magma accumulated and fractionated nickeliferous olivine and chromite in an upper-crustal staging chamber hosted by Proterozoic basement rocks. Magma then ascended and deposited olivine-chromite cumulates at the level of the complex. Prolonged magma flux in the staging chamber instigated the assimilation of basement rocks, triggering sulphide saturation and the crystallisation of Ni-poor olivine. Contaminated magma then ascended and intruded pre-existing cumulates, depositing sulphide melt that may have backflowed as magmatic activity waned. Basaltic magma then flowed over the ultramafic cumulates, depositing disseminated sulphides whilst undergoing closed-system fractionation. Basal depressions and underlying feeder structures are the most prospective locations for magmatic sulphide mineralisation.

Keywords: Mount Ayliff Complex, Karoo Igneous Province, South Africa, geochemistry, magmatic sulphide, layered intrusion

1. Introduction

The Mount Ayliff Complex (MAC) of South Africa consists of a suite of mafic-ultramafic tabular intrusions of up to 1,200 m in thickness that crop out over some 800 km^2 at the southern margin of the Kaapvaal Craton (Fig. 1A; Lightfoot and Naldrett 1984; Sander and Cawthorn 1996; Marsh *et al.* 1997; 2003; Cawthorn & Kruger 2004). The complex consists of five distinct lobes, namely Insizwa, Tonti, Tabankulu, Ingeli, and Horseshoe, that may represent the erosional remnants of a possibly continuous sheet that transgressively intruded the Ecca and Beaufort Group metasedimentary rocks of the intracratonic Karoo Supergroup (du Toit 1910; Scholtz 1937; Tischler *et al.* 1981; Cawthorn *et al.* 1986). The lobes of the MAC are among the thickest (> 1 km) and most differentiated mafic-ultramafic rocks in the ~ 183 Ma Karoo Igneous Province (Bruynzeel 1957; Eales & Marsh 1979; Lightfoot and Naldrett 1984; Lightfoot *et al.* 1987; Marsh *et al.* 2003; Cawthorn & Kruger 2004), one of the largest continental flood basalt provinces on Earth, with an estimated original areal extent of at least 1.5-2.0×10^6 km^2 and a maximum preserved thickness of 1,650 m (Eales *et al.* 1984; Marsh *et al* 1997; Jourdan *et al.* 2005; Neumann *et al.* 2011, Heinonen *et al.* 2015). The MAC forms part of the central Karoo Igneous Province together with the main Lesotho remnant, the Springbok Flats basalts north of Pretoria, and the volcanic sequence near Mariental in Namibia (Eales *et al.* 1984; Marsh *et al.* 1997). Lavas in the central region are low-Ti tholeiites (Marsh *et al.* 2003), whereas in the marginal areas (*e.g.,* Tuli, Sabi, Nuanetsi), the compositions of lavas range from nephelinites and picrites to tholeiitic basalts and rhyolites (Eales *et al.* 1984; Duncan *et al.* 1984; Ashwal *et al.* 2021). The MAC is relatively orthopyroxene- and olivine-rich when compared with other Karoo-related hypabyssal intrusions and it possibly represents a staging chamber to the overlying basaltic lavas (Lightfoot and Naldrett 1984; Maier *et al.* 2002).

The lobes of the MAC possess similar stratigraphic sequences that have historically been divided into three zones, which from base to top include the *Basal, Central*, and *Roof* zones (Fig. 1B; Scholtz 1937). The *Basal Zone* directly overlies the metasedimentary floor rocks and chilled margin, containing variable proportions of cumulus olivine and hornfelsed country rock xenoliths, overlain by olivine-rich cumulates that are historically referred to as picrites, but could instead be classified as lherzolite and olivine gabbronorite using the IUGS scheme (Lightfoot and Naldrett 1984; Maier *et al.* 2002; Albrechtsen 2006). A troctolite unit overlies the olivine-rich cumulates at Tabankulu (Lightfoot and Naldrett 1983) and is also locally preserved at Ingeli (Maske 1966). The *Central Zone* is dominated by gabbronorite and gabbro, which consist mostly of cumulus plagioclase and intercumulus pyroxene and that locally contain cumulus olivine or intercumulus quartz (Scholtz 1937; Lightfoot *et al.* 1984; Marsh *et al.* 2003). The *Roof Zone* consists of quartz diorite and monzonite that are

only locally preserved at topographical highs at Insizwa and Ingeli, where it is overlain by hornfelsed country rocks (Scholtz 1937; Cawthorn *et al.* 1988). Where preserved, the *Roof Zone* shares a gradational contact with the underlying *Central Zone* and is believed to represent a product of differentiation (Scholtz 1937). The lateral thicknesses of the zones are variable; the *Roof Zone* thins over depressions within which the *Basal Zone* thickens and *vice versa* (Scholtz 1937)

The Insizwa lobe hosts locally significant magmatic sulphide mineralisation at its base, namely at Waterfall Gorge (~ 470,000 t at 0.3% Ni, 0.25% Cu, and 0.88 ppm Pt) as well as in the immediate metasedimentary floor rocks (Bruynzeel 1957; Lightfoot & Naldrett 1984; Maske & Cawthorn 1986; Cawthorn *et al.* 1986; Maier *et al.* 2002; Marsh *et al.* 2003). Similar but less voluminous sulphide mineralisation has been identified near the basal contact of the Insizwa lobe at several other localities, including Sidakeni, Marwaqa, KwaKanya, and Ndzongiseni (Maier *et al*. 2002). Between 1996 and 2000, Falconbridge Ventures conducted detailed mapping of the MAC and drilled several boreholes through the Insizwa lobe to explore for further magmatic sulphide mineralisation (Maier *et al.* 2002; Marsh *et al.* 2003). Within this program, traverse sampling across the Ingeli and Horseshoe lobes was completed (Albrechtsen 2006). Compared to the Insizwa lobe, the Ingeli and Horseshoe lobes have received little attention with regard to their petrogenesis and magmatic sulphide prospectivity. The ~ 800-m-thick Ingeli lobe is the second largest lobe of the MAC (Fig. 1C), whereas the ~ 50-m-thick Horseshoe lobe is the smallest (Fig. 1D). Using whole-rock and mineral chemistry, electron microscopy, and thermodynamic modelling, this study proposes that the MAC was constructed incrementally by variably-contaminated Lesotho-type basalt, which entrained olivine, chromite, and immiscible sulphide melt.

2. Petrogenesis and metallogenesis of the Mount Ayliff Complex

There are several debated aspects of the MAC, including (i) the nature and mechanism of its emplacement, (ii) the composition and differentiation of its parent magma(s), and (iii) the ore-forming processes that led to the formation of its magmatic sulphide mineralisation.

Several studies have focussed on the nature and mechanism of parent magma emplacement (*e.g.,* Maske 1996; Lightfoot and Naldrett 1983; Lightfoot *et al.* 1984; Sander and Cawthorn 1996; Ferré *et al.* 2002; Maier *et al.* 2002; Marsh *et al.* 2003). Sander and Cawthorn (1996) proposed the gabbronoritic Taylor's Koppie Dyke (TKD) as well as picritic dykes to the southwest of Tabankulu and Insizwa as possible feeder structures to the MAC (Dowsett and Reid 1967; Lightfoot and Naldrett 1983). Using gravity geophysical data, they further identified several picrite-filled structurally-controlled basins (< 200 m thick) in the

footwall of the Insizwa lobe and postulated that these may represent possible feeder locations. The Ingeli lobe occupies a basinal depression in Ecca Group metasedimentary rocks, yet a SE-verging lateral emplacement model was favoured in the absence of evidence for an underlying feeder structure (Maske 1966). At the Tabankulu lobe, a sub-vertical dyke exposed at the southwestern margin is thought to extend beneath the lobe as a feeder 'keel' (Fig. 1A; Lightfoot and Naldrett 1983). Using anisotropy of magnetic susceptibility, Ferré *et al.* (2002) suggested that the magmas parental to the MAC were episodically emplaced from the southeast to the northwest via a planar feeder dyke, such as the TKD. While Maier *et al.* (2002) and Cawthorn and Kruger (2004) argued that the TKD could not have fed the lower mineralised portion of the Insizwa lobe on the basis of its orientation and metal-poor disseminated sulphides, Marsh *et al.* (2003) suggested that the TKD could have fed the Insizwa Central Zone due to similarities in whole-rock and mineral chemistry.

It is widely accepted that the MAC, particularly the Insizwa lobe, was fed by multiple injections of compositionally distinct parent magmas. This model is based on fractionation trends in the Basal Zone, the considerable thickness and homogeneity of the lherzolite unit, and evidence of thermal metamorphism in the Central Zone as well as the distinct incompatible trace element concentrations and the $^{87}Sr/^{86}Sr$ isotopic values (0.7071-0.7086; Lightfoot *et al.* 1984) in the Basal and Central zones (Lightfoot *et al.* 1984; Cawthorn *et al.* 1986; Maier *et al.* 2002; Marsh *et al.* 2003). Although hornfels xenoliths are present at the base of the Insizwa and Ingeli lobes, Marsh *et al.* (2003) showed that the parent magmas would have to assimilate ~ 50% of their own mass in metasedimentary country rocks to attain the measured initial $^{87}Sr/^{86}Sr$ values, which is not reflected in whole-rock geochemistry. Lightfoot *et al.* (1984) also reported no correlation between initial $^{87}Sr/^{86}Sr$ values and incompatible trace element concentrations and suggested that the Basal and Central Zones cannot be reconciled by way of *in situ* magmatic processes (*e.g.,* contamination, differentiation), but by the influx of compositionally distinct magmas that were possibly contaminated prior to emplacement. Instead, rocks of the Namaqua-Natal Proterozoic basement, some 2.5 km beneath the MAC (De Decker 1981) have been proposed as a possible assimilant, due to their particularly high Sr contents and initial $^{87}Sr/^{86}Sr$ values (Eglington *et al.* 1986; Marsh *et al.* 2003)

The nature of the magma parental to the olivine-rich rocks of the Basal Zone remains controversial. Several authors believe that the magma parental to the Basal Zone was comparable in composition to typical Lesotho-type basalt that was variably charged with olivine phenocrysts (Eales and Marsh 1979; Lightfoot and Naldrett 1984; Maier *et al.* 2002; Marsh *et al.* 2003). Supercooling of this parent magma led to the formation of the chilled basal olivine gabbronorite, which then facilitated the deposition of olivine-rich cumulate rocks

via insulation. In contrast, Cawthorn and colleagues (Cawthorn 1980; Cawthorn *et al.* 1986; 1988; 1992; Cawthorn and Biggar 1993) proposed a less evolved parent magma composition on the basis of Mg-rich chilled margin rocks with up to 14 wt.% MgO, the presence of Mg-rich ilmenite and olivine (Fo_{86-87}), and relatively Ni- as well as Ir-rich sulphide compositions (expressed by high Ni/Cu and low Pd/Ir values). Cawthorn and Kruger (2004) subsequently identified the so-called Waterfall Gorge Sill as a compositional analogue of the Insizwa parent magma; a thin (< 3 m) sill with 14 wt.% MgO and 137 ppm Ni that occurs ~ 20 m beneath the Insizwa lobe.

Several studies have recognized Ni-poor olivine in the Basal Zone at Tabankulu (~ 250-1,000 ppm Ni at Fo_{72-87}; Lightfoot & Naldrett 1983), Tonti (~ 500-1,300 ppm Ni at Fo_{79-84}; Cawthorn *et al.* 1992), Horseshoe (~ 580-950 ppm Ni at Fo_{77-83}; this study), and, to a lesser degree, Insizwa (~ 1,100-1,700 ppm Ni at Fo_{76-82}; Lightfoot *et al.* 1984; Maier *et al.* 2002). The presence of Ni-poor olivine coupled with the basal occurrence of magmatic sulphide mineralisation (*i.e.,* Waterfall Gorge) has been ascribed to pre-emplacement segregation and upward entrainment of sulphide melt (Lightfoot *et al.* 1984). The presence of globular sulphides in the Insizwa chilled margin rocks is consistent with this model (Tischler *et al.* 1981; Lightfoot *et al.* 1984). Small degrees of sulphide melt segregation (*R* factors > 10,000) prior to emplacement would account for the relative depletion in platinum-group elements (PGE) of the rocks (Cu/Pd > 10,000), a feature also characteristic of Karoo lavas of the Barkly East Formation in southern Lesotho (Maier *et al.* 2001). However, Maier *et al.* (2002) proposed that sulphide melt saturation at Insizwa was attained primarily *in situ* by way of differentiation and that sulphide melt penetrated downwards as evidenced by the presence of subvertical sulphide veins in the chilled rocks.

3. **Materials and methods**

Geological mapping and sampling were completed in the autumn of 2000. Grab samples of the Ingeli (0-797 m traverse) and Horseshoe (0-46 m traverse) lobes were acquired *in situ* and sampled along traverses from the base to the top of the exposed portion of the lobes. Transmitted and reflected light microscopy was conducted at Cardiff University using a Leica MZ12s microscope with a camera attachment. High-spatial resolution element maps were also produced at Cardiff University using a Carl Zeiss Sigma HD Analytical Field Emission Gun Scanning Electron Microscope equipped with two Oxford Instruments 150 mm^2 energy dispersive spectrometers (see Smith *et al.* 2023).

The composition of major silicates (olivine, orthopyroxene, clinopyroxene, and plagioclase) was determined using a wavelength dispersive JEOL CXA-733 Superprobe at Rhodes University, South Africa. The microprobe operated with a 30 nA beam current and a

15 kV accelerating voltage. Coefficients of variation based on repeat analysis of individual grains are ~ 0.3-3% for elements with concentrations between 5 and 50 wt.% and > 3 for elements with concentrations < 1 wt.% (see supplementary materials). The full mineral chemistry dataset is provided in the supplementary materials and summarised in Tables 1 and 2.

Whole-rock major element analysis was performed on fused glass beads at the University of Pretoria using an ARL 9400XP+ wavelength dispersive X-ray fluorescence spectrometer. The glass beads were quenched from a molten mixture of 1 g powdered sample and 6 g lithium metatetraborate flux in a 5% Au/Pt crucible at 1,000°C. Whole-rock trace element analysis was performed on corresponding pressed powder pellets. The CIPW normative compositions were computed using IoGAS Software and an Fe_2O_3/FeO value of 0.05.

Solution inductively coupled plasma-mass spectrometry (ICP-MS) was performed at the University of Cape Town using a Perkin Elmer/Sciex Elan 6000 ICP-MS equipped with an acid-resistant cross-flow nebuliser, a Ryton™ Scott-type spraychamber, and a Perkin Elmer AS90 autosampler. Standards used include BCR1 and BHVO1 and accuracy and precision are reported in the supplementary materials (as in Maier *et al.* 2013).

4. **Ingeli lobe**

The Ingeli lobe (-30°36'N 29°34'E) is the second largest lobe of the MAC (~ 16 × 5-6.5 km). It has a thickness of ~ 800 m, which consists of a ~ 465-m-thick basal zone of olivine gabbronorite and lherzolite, overlain by a ~ 350-m-thick sequence of olivine gabbronorite and gabbronorite. The basal olivine gabbronorite (~ 165 m thick) has a fine-grained chilled margin that contains rare cm-scale hornfels xenoliths. It is overlain by a ~ 300-m-thick lherzolite unit, a ~ 10-m-thick '*central'* olivine gabbronorite, a ~ 170-175-m-thick *'central'* gabbronorite, a ~ 30-35-m-thick *'upper'* olivine gabbronorite, and a ~ 120-m-thick upper gabbronorite. The upper contact with the hornfelsed Beaufort metasedimentary rocks is locally preserved, analogous to the Insizwa lobe (Maske & Cawthorn 1986). Maske (1966) described a troctolite unit overlying the lherzolite unit such as that described at Tabankulu (Lightfoot and Naldrett 1983), yet this was not identified in our sample traverse, possibly due to lack of exposure.

4.1. Petrography and mineral chemistry

Basal olivine gabbronorite: Subhedral and hopper-textured cumulus olivine grains (~ 65-75%; Fo_{81-86}; 1500-2300 ppm Ni) occur within medium-grained plagioclase (~ 15-25%; An_{60-68}), clinopyroxene (~ 5-10%; En_{47-54}), and orthopyroxene (~ 5-10%; En_{73-83}) oikocrysts. Cumulus plagioclase grains were rarely observed. The rocks show no evidence for

significant alteration or deformation. Olivine grains frequently host sub-circular polymineralic inclusions (< 200 μm in diameter) that are interpreted as melt inclusions (Fig. 2A-C). The inclusions variably comprise feldspar, pyroxene, phlogopite, quartz, apatite, chromite, ilmenite, and zircon. Fine-grained euhedral to subhedral chromite grains (~ 2-3%) form chains within olivine, or clusters of slightly coarser cumulus grains in the interstices of the olivine framework (Fig. 2A-C), typically in close association with intercumulus phlogopite (~ 2-3%). Anhedral apatite and Fe-Ti oxides are common accessory phases that are present in the olivine-hosted inclusions as well as amongst intercumulus minerals. Cumulus sulphides mostly occur within the olivine interstices together with chromite and were very rarely observed within olivine-hosted melt inclusions. The sulphide assemblage (~ 1-2%) consists predominantly of pyrrhotite, flame-textured and granular pentlandite, and subordinate chalcopyrite.

Lherzolite unit: Euhedral, subhedral, and hopper-textured cumulus olivine grains (~ 75-85%; Fo_{82-86}, 1300-2400 ppm Ni) occur within medium- to coarse-grained clinopyroxene (~ 5-10%; En_{49-55}) and orthopyroxene (~ 5-10%; En_{81-86}) oikocrysts (Fig. 2D), as well as medium-grained plagioclase (~ 5-10%; An_{50-70}) oikocrysts. As in the *basal olivine gabbronorite*, olivine grains enclose polymineralic melt inclusions and chromite chains (Fig. 2E-G), and relatively coarser cumulus chromite grains persist in the interstices of the olivine framework (Fig. 2H). Cumulus plagioclase grains (< 1 mm in length) are rarely observed. Intercumulus phlogopite (< 1%) persists throughout the intercumulus space where it is often spatially associated with cumulus chromite and blebby sulphides (pyrrhotite > chalcopyrite > pentlandite > galena; Fig. 2H)

Central olivine gabbronorite and gabbronorite: Fine- to medium-grained cumulus plagioclase (~ 60-80%; An_{66-78}) is hosted amongst medium- to coarse-grained orthopyroxene oikocrysts (~ 10-15%; En_{67-76}, forming locally sub-ophitic textures (Fig. 3A-B). In the *central gabbronorite*, orthopyroxene grains commonly host blebby clinopyroxene exsolution lamellae (*i.e.,* inverted pigeonite). Clinopyroxene oikocrysts are rarely observed in the *central olivine gabbronorite*, where instead clinopyroxene (~ 15-20%; En_{46-53}) typically manifests as intercumulus grains that are spatially associated with orthopyroxene. Fine-grained hopper-textured olivine grains (≤ 5%; Fo_{63-64}; 600-900 ppm Ni) are partially serpentinised and often rimmed by peritectic orthopyroxene. Few melt inclusions are observed in olivine. Interstitial accessory phases include phlogopite, sulphides, and apatite.

Upper olivine gabbronorite and gabbronorite: Fine- to medium-grained euhedral to subhedral cumulus plagioclase grains (~ 60-70%; An_{60-68}) with no preferred orientation occur amongst medium-grained orthopyroxene oikocrysts (~ 5-15%; En_{53-67}), forming locally

subophitic textures. Orthopyroxene oikocrysts become less common upward and intercumulus plagioclase grains were rarely observed in the uppermost samples of the *upper gabbronorite.* Inverted pigeonite and clinopyroxene occur as fine- to medium-grained intercumulus grains (~ 15-20%; En_{41-45}; Fig. 3D) that apparently become increasingly uralitized upward. Where present, fine-grained anhedral cumulus olivine grains (≤ 5%; Fo_{58-63}) are weakly serpentinised and partially rimmed by peritectic orthopyroxene (Fig. 3C). Inferred melt inclusions persist in the olivine grains. Accessory phlogopite, magnetite, and rare sulphides (pyrrhotite > chalcopyrite > pentlandite) are present and often spatially associated with one another. The modal abundance of alkali feldspar and quartz increase upward, where they sometimes display granophyric textures.

4.2. Geochemical stratigraphic variation

The *Basal Zone* of the Ingeli lobe is dominated by ~ 450 m of olivine-bearing cumulate rocks with uniform compositions (Fig. 4). The *basal olivine gabbronorite* shows a geochemical basal reversal whereby MgO, Ni_{wr}, Fo_{ol}, An_{pl}, and Mg_{px} contents broadly increase upwards, while CaO, Na_2O, and incompatible trace element concentrations decrease upwards. In this interval, Cr and Ni_{ol} contents are variable, while S and Cu concentrations are consistently low (< 500 ppm). Modal mineralogy as well as MgO, CaO, Fo_{ol}, An_{pl}, Mg_{px}, and incompatible trace element contents are uniform throughout the *lherzolite unit*. In this unit, patterns in Cr, Ni_{wr}, and Ni_{ol} contents are comparable in that they increase upwards for ~ 150 m and then decrease up to the contact with the *central olivine gabbronorite*, which itself is transitional between the ultramafic and mafic units. As Cr, Ni_{wr}, and Ni_{ol} contents decrease, S and Cu concentrations increase, which at maximum concentration (~ 2,200 ppm S at ~ 440 m) coincide with a sharp decrease in An_{pl}. Chalcophile element concentrations then sharply decrease upward into the *central olivine gabbronorite*. The major oxide and chalcophile element composition of the *central gabbronorite, upper olivine gabbronorite,* and *upper gabbronorite* (*i.e., Central Zone*) remains relatively invariable, with the exception of relatively low Cu contents in the *upper olivine gabbronorite* (< 40 ppm), indicative that this unit may correlate with the Cu-poor gabbronorite of the Insizwa lobe (see Maier *et al.* 2002). In the mafic interval, Cr, Fo_{ol}, An_{pl}, and Mg_{px} contents broadly decrease upwards, while incompatible trace element concentrations increase.

5. Horseshoe lobe

The Horseshoe lobe (-31°05'N 29°26'E) is the smallest lobe of the MAC (~ 6-7 × 4-5 km). It consists of ~ 45-m-thick olivine gabbronorite that is overlain by a ~ 5-m-thick gabbro.

5.1. Petrography and mineral chemistry

Olivine gabbronorite: Fine- to medium-grained subhedral and hopper-textured cumulus olivine (~ 40-65%; Fo_{77-81}; 300-900 ppm Ni) contain very fine-grained chromite chains and polymineralic inclusions (< 500 µm in diameter; Fig. 5A-C). The polymineralic inclusions host albite, phlogopite, quartz, ilmenite, apatite, amphibole, and sulphides and are interpreted as represent melt inclusions (Fig. 5D). Medium-grained plagioclase oikocrysts (~ 20-35%; An_{58-68}) are common towards the base of this unit, which become progressively superseded upward by fine- to medium-grain subhedral cumulus grains (Fig. 5E). Medium-grained orthopyroxene oikocrysts (~ 10-20%; En_{75-80}) form sub-ophitic textures with plagioclase and may enclose very fine-grained chromite grains and (or) blebby clinopyroxene exsolution lamellae. Orthopyroxene sometimes forms peritectic rims around olivine. Fine-grained intercumulus clinopyroxene grains (~ 5-20%; En_{52-54}) are partially uralitized and spatially associated with orthopyroxene. Cumulus chromite grains that occur in the olivine interstices (< 2%) are relatively coarser than those present within olivine and their modal abundance broadly decreases with stratigraphic height. These grains are often spatially associated with interstitial phlogopite (~ 1-3%), which in turn, are spatially associated with apatite and blebby sulphides (< 1%; < 500 µm in diameter). Sulphide blebs (Fig. 5F) comprise pyrrhotite, granular and flame-texture pentlandite, chalcopyrite, and galena together with rare traces of electrum and braggite.

Upper gabbro: Fine-grained subhedral cumulus plagioclase grains (~ 55-60%; An_{64}) interlock with intercumulus uralitized clinopyroxene grains (~ 35-40%; En_{45}; Fig. 5G) and sometimes occur within rare orthopyroxene oikocrysts (~ 1-3%; En_{66}). Intercumulus plagioclase is rarely observed. Interstitial quartz and alkali feldspar grains often form granophyric textures. Sulphide blebs and intercumulus phlogopite are rarely observed in the intercumulus space.

5.2. Geochemical stratigraphic variation

As in the Ingeli lobe, the lowermost ~ 10 m of the *Basal* Zone displays a geochemical reversal in which olivine mode as well as MgO, Cr, Ni_{wr}, Ni_{ol}, Fo_{ol}, and Mg_{px} contents broadly increase, while CaO, Na_2O, and incompatible trace element concentrations decrease (Fig. 6). In general, the whole-rock and mineral compositions of the *olivine gabbronorite* are invariable. From the base to ~ 22 m, S, Ni_{wr}, and Cu broadly increase, before gradually decreasing for the remainder of the sampled stratigraphy. The *Horseshoe gabbro* sample is marked by a sharp drop in MgO content and increase in TiO_2 content.

6. Whole-rock and isotope geochemistry

Lithophile elements: In olivine-bearing rocks of the Ingeli, Horseshoe, and Insizwa *Basal Zones* (Maier *et al.* 2002; Marsh *et al.* 2003; this study), SiO_2, TiO_2, Al_2O_3, CaO, Na_2O, K_2O,

and incompatible trace element concentrations increase with decreasing MgO, while FeOt, Cr, and Ni concentrations decrease (Figs. 7 and 8; Table 3). These trends are linear and olivine-bearing rocks generally plot along a tie-line between average Lesotho-type basalt and the average composition of cumulus olivine measured in the ultramafic rock types (Fig. 7). This and cumulate discrimination diagrams of Barnes (2021; Fig. 8A-B) indicate these rocks represent variable mixtures of cumulus olivine(±chromite) and trapped liquid that is comparable in composition to Lesotho-type basalt (Fig. 8A-B). The Horseshoe *olivine gabbronorite* is less primitive than olivine-bearing rocks of the Ingeli and Insizwa lobes, and it also possesses markedly lower Ni concentrations (Figs. 7 and 8), which is consistent with the presence of relatively Ni-poor olivine (Fig. 6).

The transition between the ultramafic and mafic units is marked by an abrupt drop in MgO (minus ~ 18 wt.%) and Ni (minus ~ 1,000 ppm) contents, as well as an abrupt increase in Al_2O_3 (plus ~ 13 wt.%) contents (Fig. 4). The Ingeli *central olivine gabbronorite* occurs at this transition, representing a mixture of cumulus olivine from the *Basal Zone* and cumulus plagioclase from the *Central Zone* with small proportions of cumulus pyroxenes, consistent with CIPW normative determinations (Figs. 4 and 7). The remaining rock types of the Ingeli *Central Zone* broadly evolve upward as indicated by increasing TiO_2 contents and evolving mineral compositions (Fig. 4). Their compositions are consistent with that of mafic cumulates, with the exception of the uppermost *upper gabbronorite* samples that are similar in composition to that of Lesotho-type basalt (Fig. 8A-B). The Horseshoe *upper gabbro* is almost identical in composition to average Lesotho-type basalt, some Insizwa chilled margin samples, and the Insizwa footwall sill (Marsh *et al.* 1997; Maier *et al.* 2002), which is best observed in their TiO_2 (~ 1 wt.%) and Al_2O_3 (~ 15 wt.%) contents (Figs. 7 and 8).

The Insizwa chilled margin and TKD (Maier *et al.* 2002; Marsh *et al.* 2003) broadly overlap in composition, yet the Insizwa chilled margin generally has higher Ni and lower incompatible trace element concentrations. The MgO, TiO_2, and Ni concentrations of the Waterfall Gorge Sill (whole-rock and glass; Cawthorn and Kruger 2004) broadly overlap with the TKD and Insizwa chilled margin, yet with relatively higher SiO_2, Al_2O_3, and CaO concentrations as well as highly variable FeOt contents (~ 5.4-11.5 wt.%). The floor rocks include basement rocks of the Namaqua-Natal mobile belt (Eglington et al. 1986; Nethenzheni 2016) and local Ecca Group metasedimentary rocks (Neumann *et al.* 2011) which have relatively low MgO, FeOt, CaO, and Ni concentrations, high SiO_2, Na_2O, K_2O, and rare earth element (REE), and variable TiO_2, Cr, and incompatible trace element concentrations (Fig. 9).

Multi-element normalised profiles: Sixteen samples from the Ingeli lobe were analysed by ICP-MS for a full suite of trace elements (Fig. 9; Table 4). The Ingeli units have comparable shallow-downward sloping primitive mantle-normalised profiles (Th/Yb_N = 3.94-6.46; La/Sm_N = 1.97-2.43), with slight negative Nb/Nb* (0.38-0.44) and Ti/Ti* (0.51-0.71), and elevated Pb concentrations. The central units have elevated Sr and Eu concentrations (Eu//Eu* = 1.40-1.57) consistent with the presence of accumulated plagioclase primocrysts. The trace element concentrations of Lesotho-type basalts are comparable to that of the Insizwa chilled margin, albeit slightly enriched relative to primitive mantle. These profiles are mostly characterised by shallow-downward slopes (Th/Yb_N = 1.40-5.09; La/Sm_N = 0.26-2.25), negative Ti/Ti* (0.43-2.12) and flat Eu/Eu* (0.81-2.12) values. The basement rocks and Ecca Group metasedimentary rocks have comparable profiles in that they are downward-sloping (Th/Yb_N = 27.2-27.5; La/Sm_N = 3.08-3.46) with pronounced negative Ti/Ti* values (0.20-0.22; Fig. 9).

Chalcophile elements: In the lower ultramafic portion of Ingeli, S shows a well-defined positive correlation with Cu (R^2 = 0.96) but not with Ni (Fig. 10A-B). In contrast, S, Ni, and Cu concentrations show strong positive inter-element correlations in the Horseshoe olivine gabbronorite and gabbro (R^2 > 0.9). This indicates that Ni concentrations in the olivine-bearing rocks of Ingeli and Horseshoe are primarily controlled by olivine and sulphides, respectively. Sulphur, Ni, and Cu concentrations do not show any systematic correlations in the upper mafic portions of Ingeli. For this reason, Ni/Cu values effectively subdivide rock units of the MAC into: (i) non-mineralised olivine cumulates (Ni/Cu > 10); (ii) mineralised olivine cumulates (10 > Ni/Cu > 3); (iii) non-mineralised gabbronoritic-gabbroic units (Ni/Cu < 3; Fig. 10C). Sulphur, Ni, and Cu concentrations have strong positive inter-element correlations in the TKD (R^2 > 0.96; *n* = 4). There are too few samples of the other possible parent magma compositions to assess correlations. In general, most of the MAC units and possible parent magma analogues have Cu/Zr values at or below 1 (Fig. 10D), which suggests some degree of sulphide melt accumulation. The basement rocks and Ecca Group metasedimentary rocks have low chalcophile element concentrations and Cu/Zr values mostly below 0.2.

Summary of Sr-isotopic data: Though we do not present new isotopic data in this study, we deem it pertinent to describe existing isotopic data for the MAC and related intrusions here in the context of our data, in order to refine the petrogenetic model. When recalculated to 183 Ma (Duncan *et al.* 1984), $^{87}Sr/^{86}Sr_{(i)}$ values of the Insizwa lower rocks range from 0.70596 to 0.71078, while the Insizwa upper rocks range from 0.70478 to 0.71089 (Lightfoot *et al.* 1984; Maier *et al.* 2002; Cawthorn and Kruger 2004; Fig. 11). The Insizwa chill and footwall hornfels have $^{87}Sr/^{86}Sr_{(i)}$ values of 0.70869 and 0.71232, respectively. Volcanic rocks of the

Karoo igneous province have $^{87}Sr/^{86}Sr_{(i)}$ values ranging from 0.70489 to 0.70841 (10^{th} to 90^{th} percentile; Marsh *et al.* 1997; Jourdan *et al.* 2007; Neumann *et al.* 2011), where Lesotho-type basalts have an average $^{87}Sr/^{86}Sr_{(i)}$ value of 0.70566 ± 89 (*n* = 13; Marsh *et al.* 1997).

7. Discussion

7.1. Nature of the parent magma(s)

It remains debated as to whether the MAC was incrementally constructed by Lesotho-type basalt (~ 7 wt.% MgO) charged with variable proportions of olivine phenocrysts (Eales and Marsh 1979; Lightfoot and Naldrett 1983, 1984; Marsh *et al.* 2003) or by relatively tholeiitic magma (particularly the lower olivine-bearing rocks) with > 10 wt.% MgO (Cawthorn 1980; Cawthorn *et al.* 1992; Cawthorn and Kruger 2004). Episodic top-down construction by compositionally distinct magmas has been proposed for the Insizwa lobe of the MAC, whereby the basal olivine-bearing rocks were deposited by olivine-charged doleritic magma after the formation of the upper units by a magma comparable in composition to the TKD (Marsh *et al.* 2003). Ultramafic intrusive rocks are volumetrically rare in the Karoo Igneous Province, with most instances of high-Mg picrites occurring in the marginal rift-related areas, such as Lebombo, Tuli, and Mwenezi (Eales *et al.* 1984). It is believed that Karoo picrites with < 18 wt.% MgO are essentially liquids due to their glassy nature and dearth of olivine phenocrysts (Bristow and Cox 1984). Alternatively, Ashwal *et al.* (2021) argued that Lebombo-Mwenezi picrites represent mixtures of olivine phenocrysts and evolved Sr-rich basaltic-trachyandesitic to dacitic melts. Other mafic-ultramafic intrusions in the region include the Elephant's Head Dyke and New Amalfi Sheet, with the former being the putative feeder to the latter (Poldervaart *et al.* 1943; Williams 1995). It was proposed that tholeiitic and olivine-charged doleritic magma fluxed through the Elephant's Head Dyke, yet only olivine-charged doleritic magma constructed the New Amalfi Sheet and its picritic units reflect olivine accumulation.

In the MAC, *Basal Zone* lithologies are geochemically consistent with first-order mixing of olivine-chromite cumulates and liquid that is compositionally comparable to that of Lesotho-type basalt (Fig. 7). By considering S-poor (< 0.15% S) olivine-chromite cumulate samples, one can approximate the composition of the parent melt using the method detailed by Chai and Naldrett (1992). This method utilises whole-rock FeOt concentrations and, thus, disregards the small proportion of Fe_2O_3 present in chromite, which otherwise leads to slight underestimations of whole-rock Mg# number. Using an Mg-Fe exchange coefficient (0.3 ± 0.03; Roeder and Emslie 1970), Lightfoot and Naldrett (1984) showed that the most forsteritic olivine ($Fo_{82.5}$) then known from Tabankulu and Waterfall Gorge was in equilibrium with Lesotho-type basalt and that subtraction of cumulus olivine from the chilled units also yields a composition comparable to that of Lesotho-type basalt. However, a complication is

that the composition of cumulus olivine may be modified as it equilibrates with trapped interstitial liquid and/or immiscible sulphide melt (Barnes 1986; Cawthorn *et al.* 1992; Li and Naldrett 1999). While the generally low proportion of sulphides, particularly at Ingeli, precludes significant Fe-Ni exchange between olivine and sulphide melt, Cawthorn *et al.* (1992) argued that trapped liquid shift is responsible for lowering the Fo contents of cumulus olivine in the Insizwa *Basal Zone* by up to 9 mol.% and that the true parental magma contained 10.8 wt.% MgO at 10.5 wt.% FeO.

Simple first-order mixing calculations show that the whole-rock compositions of *Basal Zone* rocks can be replicated by mixing 60-80% olivine with 20-40% liquid that has a composition of Lesotho-type basalt (Fig. 7). Conversely, incremental removal of olivine from the Insizwa chilled margins leads to a residual liquid comparable in composition to Lesotho-type basalt (Lightfoot and Naldrett 1984; Marsh *et al.* 2003). It has been noted that the major oxide composition of the Insizwa and Tonti *Basal Zone* olivine-chromite cumulates define linear arrays that project to Fo_{85-87} (Cawthorn *et al.* 1992; Marsh *et al.* 2003). This remains true for the Ingeli *Basal Zone*, though, the overall poor correlation between MgO and FeOt reduces the reliability of parent magma determinations (Fig. 12A). In fact, in the S-poor Ingeli *lherzolite unit* samples, MgO and FeOt negatively correlate ($R^2 = 0.66$), which is perhaps most consistent with trapped liquid shift when considering the olivine compositions and the absence of fractionation trends in the *Basal Zone* (Fig. 4). Although MgO and FeOt positively correlate in the Ingeli basal reversal samples ($R^2 = 0.95$), they define a trend that projects to implausibly low FeOt concentrations for the parent melt and, instead, may represent the composition of the residual liquid following re-equilibration with olivine.

Since this method relies on olivine being the only cumulus phase, a correction should be applied to account for the presence of cumulus plagioclase in the Horseshoe *olivine gabbronorite* (Fig. 5E), for without correction, it too projects to implausibly low FeOt contents for a given MgO content (Fig. 12B; Li *et al.* 2000). If a conservative proportion (50% of the CIPW normative determination) of cumulus plagioclase is removed from each sample, the major element concentrations define an array between the most forsteritic olivine measured at Horseshoe ($Fo_{80.6}$) and a liquid with 6.67 wt.% MgO and 6.50 wt.% FeOt. This composition is similar to Lesotho-type basalt as well as the overlying Horseshoe *upper gabbro* (Fig. 12B). The same analysis on available data for the Taylor's Koppie Dyke (Marsh *et al.* 2003) yields similar results, yet this is poorly constrained in the absence of petrographic observations. Nonetheless, whole-rock and mineral chemical signatures of the Horseshoe *olivine gabbronorite* are similar to that of Taylor's Koppie Dyke (also olivine gabbronorite), which itself has been previously petrogenetically linked to the Insizwa *Central Zone* on the basis of similar observations (Marsh *et al.* 2003). In summary, Lesotho-type

basalt appears to be parental to Horseshoe and it is apparent that Ingeli *Basal Zone* cumulates represent first-order mixtures of olivine-chromite cumulates and Lesotho-type basalt. However, Ingeli olivine (and Insizwa) requires a less evolved parent magma composition as well as entrainment from elsewhere prior to undergoing some degree of re-equilibration.

7.2. Thermodynamic modelling and crustal contamination

7.2.1. Parameterisation of intensive variables

AlphaMELTS 1.9 (Ghiorso and Sack 1995) was used to produce thermodynamically constrained forward models of the magma compositions considered to be parental to the MAC. In the central Karoo basin, relatively thick sills with overlying dyke-sill networks were emplaced at paleo-depths of 700 to 1,000 m, corresponding to emplacement pressures of ~ 20 to 25 MPa (Coetzee and Kisters 2020). Neumann *et al.* (2011) effectively modelled the composition of Karoo dolerites by fractional crystallisation of sample QU1-1-9 (7.7 wt.% MgO) under low pressures (500 bars) and oxidising (ΔFMQ+1) conditions. Neumann *et al.* (2001) further stated that the parent magma may have assimilated small proportions of country rocks, such as Ecca Group metasedimentary rocks, as well as experienced up to 10% assimilation of basement rocks at depth.

Despite the presence of hornfelsed xenoliths at the base of the Insizwa and Ingeli lobes (Lightfoot *et al.* 1984; this study), significant local country rock assimilation has been rejected by previous researchers due to the disparity between incompatible trace element concentrations, S isotopes, and $^{87}Sr/^{86}Sr_{(i)}$ isotopic compositions (Tischler *et al.* 1981; Lightfoot *et al.* 1984; Marsh *et al.* 2002). Assimilation of Namaqua-Natal basement rocks at depth, however, is a possible alternative given their relatively high Sr (up to 826 ppm) and $^{87}Sr/^{86}Sr_{(183\ Ma)}$ (0.76406) compositions (Eglington et al. 1986; Eglington and Armstrong 2003; Bailie *et al.* 2017). Some studies have further proposed that a contamination event at greater depths might have triggered pre-emplacement sulphide melt segregation (Cawthorn 1980; Tischler *et al.* 1981; Lightfoot *et al.* 1984). The lithostatic pressure at the depth of the basement rocks was estimated to be ~ 100 MPa using a density of 2.7 g/cm^3 and a depth of 4 km, which is reasonable given that the basement rocks occur ~ 2.5 km beneath the MAC (De Decker 1981). The average heat flow in the southern portion of the Karoo basin is 62 ± 11 mW m^{-2} at the southern margin (Jones and Scheiber-Enslin 2022). Using the geothermal model of Hasterok and Chapman (2011) and the local average heat flow, the temperature of the basement and metasedimentary country rocks prior to melt infiltration are estimated to be 80°C and 20°C, respectively. These temperatures were used in models considering assimilation.

The presence of cumulus olivine in the Insizwa chilled margin and TKD suggests that these rocks are not analogous to true parent magma compositions. At the emplacement level, the parent magmas considered were the Insizwa footwall sill (Maier *et al.* 2002), the Waterfall Gorge Sill (Cawthorn and Kruger 2004), and Karoo dolerite sample QU1-1-9 (Neumann *et al*. 2011; Barnes and Mansur 2022; Table 5). There is no $^{87}Sr/^{86}Sr_{(i)}$ value reported for sample QU1-1-9, but comparable sample QU1-1-4 has an $^{87}Sr/^{86}Sr_{(i)}$ value of 0.70566 (Neumann *et al.* 2011). This value is within the range reported for the Insizwa *Central Zone* (0.70478 to 0.70789; Maier *et al.* 2002; Cawthorn and Kruger 2004) and is used in the thermodynamic modelling. As Neumann *et al.* (2011) suggests that Karoo dolerites have experienced fractionation and up to 10% assimilation of basement rocks at depth prior to emplacement (see also Heinonen *et al.* 2015; Barnes and Mansur 2022), 10 g of Proterozoic basement rock was removed from sample QU1-1-9 using the method of Mungall *et al.* (2010). This 'uncontaminated' QU1-1-9 composition (Table 5) has an $^{87}Sr/^{86}Sr_{(i)}$ value of 0.70449 (Table 5), which is consistent with the lower range reported for a subset of Lesotho-type basalts.

Batch and fractional crystallisation scenarios at conditions of 0.5 wt.% H_2O, 20 MPa, and ΔFMQ+1, with and without the assimilation of Ecca Group metasedimentary rocks were considered. The effect of pre-emplacement assimilation of Proterozoic basement rocks at 100 MPa was also considered. The best fit between the model output and measured data was sought by way of weighted least squares regression combined with the *Solver Function* of Microsoft Excel™. The QU1-1-9 dolerite models produced the best fit to the measured data and these models are described here (Table 5). The model inputs and outputs are reported in the supplementary materials and the modelled compositions are compared with measured rocks in Table 6.

7.2.2. Modelling the Ingeli *Central Zone*

The Ingeli *Central Zone* units were best modelled during low-pressure (200 bars) fractional crystallisation of the QU1-1-9 dolerite. In this model, spinel is the first phase on the liquidus at 1200°C, followed by olivine (Fo_{83-79}) at 1178°C. Plagioclase (An_{80-54}) and clinopyroxene join olivine on the liquidus at 1162°C. Olivine is replaced by orthopyroxene (Mg_{79-66}) at 1136°C. The mineral compositions closely resemble those measured in the Ingeli *Central Zone* (Fig. 4). The average composition of the Ingeli *central gabbronorite* is best replicated as gabbronoritic mesocumulates (14:86 liquid:solid at 1124°C), where the cumulates comprise 52% plagioclase, 30% clinopyroxene, and 18% orthopyroxene and the trapped liquid is comparable in composition to average Lesotho-type basalt (Mg_{63}; Table 6; Figs. 13 and 14A). The $^{87}Sr/^{86}Sr_{(i)}$ value remains unfractionated (0.70566), and the modelled whole-

rock and plagioclase Sr concentrations are 190 ppm and 389 ppm, respectively. These values are consistent with those measured in the Insizwa *Central Zone* (Fig. 15A; Cawthorn and Kruger 2004). Simply mixing the unevolved QU1-1-9 composition with 0-20% Proterozoic basement rocks (sample Kan1; Bailie *et al.* 2017) yields an $^{87}Sr/^{86}Sr_{(i)}$ range of 0.70449 to 0.70676 that is also within the range of values reported for the Insizwa *Central Zone* (Fig. 15B).

7.2.3. Modelling the Ingeli and Horseshoe *Basal Zones*

The Horseshoe and Ingeli *Basal Zone units* were best replicated by a model of low-pressure fractional crystallisation of the QU1-1-9 dolerite that had been contaminated at depth by 6 g of Proterozoic basement rocks (Table 6). The pre-emplacement assimilation of Proterozoic Namaqua-Natal basement rocks, such as Port Edward enderbite (Eglington et al. 1986), can significantly increase the Sr contents and $^{87}Sr/^{86}Sr_{(i)}$ compositions of the proposed MAC parent magma (Fig. 15), while not significantly affecting its trace element contents (Fig. 14). Such a process could be important at the Insizwa lobe where the *Basal Zone* units possess a more radiogenic $^{87}Sr/^{86}Sr_{(i)}$ composition relative to the *Central Zone* units (Lightfoot *et al.* 1984; Maier *et al.* 2002; Cawthorn and Kruger 2004). During pre-emplacement assimilation-batch crystallisation of the QU1-1-9 dolerite, only small proportions of spinel and Mg-silicates had crystallised, while the $^{87}Sr/^{86}Sr_{(i)}$ composition of the liquid had increased from 0.70566 to 0.70709 (Fig. 15). Modelling low-pressure fractional crystallisation of this contaminated magma (Table 5), olivine (Fo_{83-75}) and spinel are eventually joined on the liquidus by clinopyroxene at 1142°C and plagioclase (An_{81-36}) at 1130°C. Olivine is replaced on the liquidus by orthopyroxene (Mg_{76-62}) at 1094°C. The average composition of the Ingeli *basal olivine gabbronorite* and *lherzolite unit* were best replicated as olivine-chromite orthocumulates and mesocumulates, respectively (Figs. 13 and 14B; Table 6). The $^{87}Sr/^{86}Sr_{(i)}$ value of the modelled units (0.70709) are relatively low compared to those reported for the Insizwa *Basal Zone* (Maier *et al.* 2002; Cawthorn and Kruger 2004), yet the Sr contents of the modelled *basal olivine gabbronorite* (68 ppm) and its plagioclase component (444 ppm) are consistent with the measured data (Fig. 15). The Horseshoe *olivine gabbronorite* was best replicated as an olivine-chromite orthocumulate at 1156°C (Figs. 13 and 14C; Table 6). Moreover, the average composition of the Insizwa *chilled margin* was best replicated as 13% olivine and 87% contaminated liquid that is comparable in composition to average Lesotho-type basalt (Fig. 14C).

7.3. Olivine compositions

Three groups of olivine are identified in the MAC: (1) Ni-rich (> 1200 ppm) and forsteritic (> 70 mol.%) grains that predominantly occur in the Insizwa and Ingeli *Basal Zones*; (2) Ni-poor

(< 1200 ppm) and forsteritic (> 70 mol.%) grains that predominantly occur in the Horseshoe, Tonti, and Tabakulu *Basal Zones*, as well as the TKD, Waterfall Gorge Sill, and Insizwa *Basal Zone*; (3) the relatively less forsteritic (< 72 mol.%) grains that predominantly occur in the Insizwa, Ingeli, and Tabakulu *Central Zones* (Fig. 16A). The Ni content of *Basal Zone* olivine grains for a given forsterite content broadly decreases southwards, with the exception of putative feeder structures that consistently have Ni-poor forsteritic olivine (*i.e.,* TKD, Waterfall Gorge Sill, Tabankulu Feeder; Fig. 16). These grains are Ni-poor relative to olivine from barren intrusions associated with large igneous provinces (Fig. 16B; Barnes *et al.* 2023) and can be considered a favorable indicator for the presence of accumulated sulphide somewhere in the MAC plumbing system.

Batch crystallisation of the uncontaminated QU1-1-9 dolerite (Table 5) at 1 kbar and ΔFMQ+1 was modelled to replicate the measured olivine compositions (Fig. 16C). The $D^{Ni/Liq}$ values for olivine, orthopyroxene, and clinopyroxene were calculated using the models of Matzen *et al.* (2017), Beattie *et al.* (1991), and Bedard (2014), respectively. The modelled olivine forsterite contents (Fo_{84-60}) are consistent with the forsterite contents of olivine from groups 1 and 3. However, to generate sufficient Ni contents, ~ 125 ppm Ni is required in the starting composition, which is greater than that estimated for the uncontaminated QU1-1-9 dolerite (~ 94 ppm). The Insizwa footwall sill (Maier *et al.* 2002) and volcanic rocks of the Barkley East Formation (*e.g.,* Roma, Sani, Golden Gate; Marsh *et al.* 1997) have the MgO, FeO, and Ni contents required to replicate the MAC olivine compositions.

Group 2 olivine grains are too Ni-poor to be modelled by S-undersaturated crystallisation and, instead, require either coprecipitation with sulphide melt or precipitation from a melt that has previously experienced sulphide melt extraction (Barnes *et al.* 2023). Several authors have proposed that the parent magma(s) have previously experienced segregation of small proportions of sulphide melt (discussed below; Tischler *et al.* 1981; Lightfoot *et al.* 1984). Closed-system batch equilibration of silicate magma (10:1 liquid:olivine) with sulphide melt at *R*-factors ranging from 100-1,000 can effectively produce the Group 2 olivine grains (Barnes *et al.* 2013; 2023). However, the homogeneity of *Basal Zone* cumulates across the MAC is most consistent with having been formed by the shedding of entrained cumulus phases (*e.g.,* olivine, spinel ± sulphide melt) during repeated influxes of parent magma in an open-system. The presence of globular sulphides in the Insizwa *Basal Zone* and the occurrence of sulphides in olivine-hosted melt inclusions, particularly at Horseshoe (Figs. 2G and 5D), suggests that these phases coprecipitated upstream and were transported to their current location. The Group 2 olivine grains can be effectively modelled by S-saturated batch crystallisation, whereby olivine:sulphide proportion ratios range from 50-500 (Fig. 16C),

consistent with conclusion that MAC sulphides formed at variable *R*-factors (Maier *et al.* 2002).

While the uncontaminated QU1-1-9 dolerite composition can accommodate most measured olivine compositions, there are some less evolved olivine grains present only in the Insizwa and Ingeli *Basal Zones* (*i.e.,* the northernmost lobes). These grains can be replicated by back-fractionation of the uncontaminated QU1-1-9 dolerite when the melt has attained an Mg# value of 68 mol.% and 349 ppm Ni (Fig. 16C). It is proposed that these grains precipitated from a primitive and S-undersaturated melt at depth and were subsequently deposited at the level of the MAC by relatively evolved melts; there is no clear evidence for the existence of high-Mg magmas at the level of the MAC. It is likely that cumulus olivine grains underwent some degree of trapped liquid shift (Cawthorn *et al.* 1992), in the presence or absence of sulphide melt (Fig 16C).

7.4. Segregation of sulphide melt and implications for magmatic sulphide prospectivity

Low-pressure basaltic magmas typically need to undergo high degrees of fractionation and (or) assimilate exogeneous sulphur to become saturated in sulphide melt (Mavrogenes and O'Neill 1999; Ripley and Li 2013; Smythe *et al.* 2017). Sulphide mineralisation at Waterfall Gorge is mostly confined to the interstices of the basal units (Lightfoot *et al.* 1984). The sulphides possess mantle-like $\delta^{34}S$ values (-4 to +4‰) and low PGE contents relative to base metals (Jensen 1967; Lightfoot *et al.* 1984; Maier *et al.* 2002). These observations have led researchers to propose that the sulphides are of magmatic origin but segregated from PGE-depleted magma, suggesting that a previous episode of sulphide melt segregation may have occurred at depth (Tischler *et al.* 1981; Lightfoot *et al.* 1984; Cawthorn and Kruger 2004). While this conclusion is consistent with the presence of Ni-depleted olivine in the Horseshoe, Tabankulu, Tonti, and southern Insizwa lobes as well as possible feeders (*e.g.,* Taylor's Koppie Dyke), relatively Ni-rich olivine persists in lherzolitic units of the Tabankulu, Insizwa, and Ingeli lobe (Lightfoot and Naldrett 1983; Lightfoot *et al.* 1984; Cawthorn *et al.* 1992; Marsh *et al.* 2003; this study). This attests to the influx of at least two pulses of olivine-saturated magma that had experienced different degrees of sulphide melt saturation.

In the Ingeli lobe, whole-rock S and Cu concentrations peak beneath the *Basal-Central Zone* (*e.g.,* mafic-ultramafic) transition and gradually decrease downwards for some ~ 150 m, antithetical to whole-rock Cr contents as well as Ni concentrations in both whole-rock and olivine (Fig. 4). Considering the absence of Ni-depleted olivine (Fig. 16C) and rarity of sulphide-bearing olivine-hosted melt inclusions (Fig. 2E-G), it is concluded that the lower ~ 300 m of the Ingeli ultramafic rocks were deposited by multiple surges of S-undersaturated (or very sulphide-poor) and olivine-charged doleritic magma. The upper ~ 340 m of the Ingeli

lobe is thought to represent closed-system fractionation of a distinct pulse of doleritic magma as evidenced by the upward increasing incompatible trace element concentrations and upward decreasing Cr, Ni, An_{pl} and Mg_{px} contents (Figs. 4 and 17). The implication of this model is that basal sulphide accumulations of the MAC (*i.e.,* Waterfall Gorge) are petrogenetically separate from stratiform sulphide accumulations at the mafic-ultramafic transition in the Ingeli and Insizwa lobes (Maier *et al.* 2002; this study), but detailed analyses are currently unavailable.

Lesotho-type basalts have low S concentrations (~ 200 ppm on average), which likely reflects depressurisation-induced degassing (Métrich and Wallace 2008; Barnes and Mansur 2022). Using the model of Smythe *et al.* (2017), a the QU1-1-9 magma with 200 ppm S would attain SCSS after > 50% fractional crystallisation, inconsistent with the occurrence of sulphides at the mafic-ultramafic transition of Ingeli and Insizwa. If the magma contains > 700 ppm S, which is typical of basaltic magmas (Wallace and Carmichael 1992), sulphide melt precipitates shortly after olivine. In this scenario, cotectic portions of sulphide melt would gravitationally settle at the mafic-ultramafic transition and percolate downward into the underlying mushy cumulates somewhat analogous to the Merensky Reef of the Bushveld Complex (Naldrett *et al.* 2009; Smith *et al.* 2021A) and Huckleberry Sill Complex of Labrador (Smith *et al.* 2021B). While this may explain the stratiform sulphide occurrences at the Ingeli and Insizwa mafic-ultramafic transition, it cannot explain the basal sulphide accumulations at Waterfall Gorge or the blebby sulphides throughout Horseshoe.

Isolated sulphide blebs are present throughout the Horseshoe stratigraphy and sulphides were regularly observed within olivine-hosted melt inclusions (Fig. 5D). Sulphur and chalcophile metals strongly correlate positively in the Horseshoe lobe (Fig. 10) and all olivine grains are relatively Ni depleted (Figs. 16). These observations are consistent with olivine and sulphide melt coprecipitating at depth from the Horseshoe parent magma, prior to entrainment and subsequent deposition at the level of the MAC. There is no textural or geochemical evidence for the percolation of sulphide melt at Horseshoe, which may have been hampered by the porosity of the cumulates and/or the ability for the sulphide to wet the cumulus phases (Mungall and Su 2005) and (or) the rapid cooling of a relatively thin (~ 50 m) sill. As the Insizwa lobe is > 10 times thicker than Horseshoe, a model of sulphide entrainment, deposition, and percolation is feasible for the basal sulphide accumulations at Waterfall Gorge, as described by Lightfoot *et al.* (1984)

Basal sulphide accumulations were not identified in the Ingeli lobe, however, only one traverse was analysed and the southern portion of the Ingeli lobe remains unstudied – Group 2 Ni-depleted olivine grains may be found here, which would increase its potential for basal

sulphide accumulations. While not identified in drilling programmes of Falconbridge, basal depressions within which sulphide may accumulate remain the best targets in the MAC, particularly in the southern lobes. Sander and Cawthorn (1996) postulated that trough-like basal depressions in the Insizwa lobe were feeder structures and Lightfoot and Naldrett. (1983) documented an olivine-choked subvertical dyke at the base of the Tabankulu lobe that was interpreted as the feeder keel. If these assumptions are true, these structures would ultimately resemble ultramafic plugs within which immiscible sulphide melt may percolate down upon the cessation of magmatic activity (Hughes *et al.* 2016; Mao *et al.* 2018). Since magmas cannot entrain large amounts of dense sulphide melt over prolonged distances (Robertson *et al.* 2015), it is also plausible that the known basal sulphide accumulations do not represent all the sulphide melt that was entrained. Both of these processes would explain why the documented volume of magmatic sulphide accumulation in the MAC is not sufficient as to account for the Ni inferred to have been lost from the lherzolitic units (*e.g.,* Lightfoot *et al.* 1984).

7.5. Petrogenetic model and global analogues

The MAC represents a once continuous mafic-ultramafic sill-like intrusion that was constructed incrementally by Karoo doleritic magmas that were variably charged with olivine, chromite, and sulphide melt. We build on the petrogenetic models described in previous literature by incorporating each of the isolated lobes into a unified model (Fig. 17), allowing us to critically examine controversial aspects of the MAC, including (i) the composition and mineral cargo of the parent magmas; (ii) the emplacement mechanism and construction sequence; (iii) the role of contamination; (iv) the spatial distribution of Ni-rich and Ni-poor olivine; (v) the timing of sulphide melt saturation. The following sequence of events is proposed:

1. Upwelling Karoo doleritic melt (Mg# > 60 mol.%) arrived in an upper crustal staging chamber hosted within Sr-rich Proterozoic basement rocks, such as those reported in the Namaqua-Natal mobile belt (Eglington et al. 1986; Bailie *et al.* 2017). The melt became saturated in chromite and then olivine, whereby Ni strongly partitioned into olivine in the absence of immiscible sulphide melt. Melt entraining olivine and chromite was progressively ejected upward from the upper crustal chamber via NNW-SSE-oriented structures (Cawthorn and Kruger 2004). Olivine- and chromite-charged magmas continuously fluxed at the level of the MAC via underlying feeder structures (*i.e.,* Tabankulu feeder; Lightfoot and Naldrett 1983) and progressively deposited ultramafic cumulates of the Insizwa and Ingeli lobes. Small proportions of sulphide melt were likely entrained at this stage due to the presence of minor disseminated sulphides and sulphide-bearing olivine-hosted melt inclusions in the Ingeli *Basal Zone,* though *R*-factors

would have been sufficiently high as to not significantly impact the Ni content of coexisting olivine.

2. Progressive influx of melt into the upper crustal staging chamber combined with the latent heat of fusion allowed the magma to begin assimilating the Proterozoic basement rocks, thus, increasing its $^{87}Sr/^{86}Sr_{(i)}$ composition (Marsh *et al.* 2003; Cawthorn and Kruger 2004). This led to sulphide melt segregation in the staging chamber, causing subsequently crystallising olivine to be relatively Ni-depleted. The contaminated magma, now entraining relatively Ni-poor olivine and sulphide melt, intruded pre-existing olivine cumulates of the northern MAC (*i.e.,* Insizwa ad Ingeli) and contaminated melt displaced the resident intercumulus liquid (Sander and Cawthorn 1995). The crystal-charged contaminated magma further constructed the *Basal Zones* of the south-central MAC (*i.e.,* Tonti, Tabankulu, and Tonti). Where possible, entrained sulphide melt percolated downward and concentrated within basal depressions (*i.e.,* Waterfall Gorge) and some possibly backflowed down feeder structure as magmatic activity waned (Lightfoot and Naldrett 1983; Hughes *et al.* 2016).
3. A separate pulse of uncontaminated basaltic magma entered the chamber laterally, flowing over the resident olivine-rich mush deposited by antecedent pulses of magma (Lightfoot and Naldrett 1983). Upon the cessation of magmatic activity, the remaining melt underwent closed-system fractionation and became saturated in sulphide melt by way of differentiation (Maier *et al.* 2002). This model = is supported by the distinct $^{87}Sr/^{86}Sr_{(i)}$ compositions and sulphide accumulation at the sharp mafic-ultramafic transition recorded in the Insizwa and Ingeli lobes (Maier *et al.* 2002; this study). These sulphides may be chemically and isotopically distinct from basal sulphide accumulations (*i.e.,* Waterfall Gorge).

Several other contemporaneous olivine-bearing doleritic intrusions exist near to the MAC, including the Elephant's Head Dyke, New Amalfi Sheet, Mount Arthur Complex, and Birds River Sill (Poldervaart and Walker 1943; 1948; Eales 1990 Williams 1995). The former three intrusions possibly occur along an inferred NW-SE-oriented lineament that also intersects the MAC (Sander and Cawthorn 1996). This, and other established NE-SW structures, facilitated the emplacement of olivine-charged doleritic magma that constructed, at least in part, each of the intrusions (Poldervaart and Walker 1946). While the New Amalfi Sheet and Birds River Sill resemble unprospective olivine-poor and highly fractionated sheet intrusions, the Elephant's Head Dyke and Mount Arthur Complex are inferred as feeder structures that record multiple fluxes of distinct olivine-bearing magmas (Poldervaart and Walker 1943; 1946), like that described for the MAC (Lightfoot *et al.* 1983; Marsh *et al.* 2003; this study). Thick picrites are observed only in the Elephant's Head Dyke (Fo_{83-81}), yet there is presently

no knowledge of its Sr-isotopic composition or olivine Ni contents (Poldervaart and Walker 1943; Williams 1995). Collectively, each of these intrusions may have been incrementally constructed southeastward, whereby contaminated sulphide-bearing magma upwelled in the central-southern portions of the MAC.

The MAC has a similar inferred petrogenetic history to that of chonolithic intrusions, such as South Africa's ~ 2.05 Ga Uitkomst intrusion and Canada's Current Lake intrusion (Gauert *et al.* 1995; Maier *et al.* 2018; Brzozowski *et al.* 2023). Both of these conduit-hosted intrusions comprise thick olivine-rich cumulates and basal sulphide accumulations inferred to have been constructed incrementally by progressively influxing olivine- and sulphide-charged magmas. Upon the cessation of magmatic activity, the systems underwent closed-system fractionation, during which, mobile olivine- and sulphide-rich slurries may have back-flowed and accumulated in the feeder structure (Gauert *et al.* 1995; Brzozowski *et al.* 2023), such as that described at the Tabankulu lobe of the MAC (Lightfoot and Naldrett 1983). In each case, crustal contamination is thought to have played a central role in ore genesis (Maier *et al.* 2018; Brzozowski *et al.* 2023), whereby the absence of S-rich country rocks in proximity to the MAC may have restricted its ore-forming potential.

8. **Conclusions**

The ~ 183 Ma Mount Ayliff Complex (MAC) of South Africa's Karoo Igneous Province was constructed by multiple pulses of variably contaminated doleritic magma that entrained a cargo of olivine, chromite, and immiscible sulphide melt. It is suggested that the MAC was once a continuous sill-like intrusion that is now represented by five distinct lobes named Insizwa, Tabankulu, Tonti, Ingeli and Horseshoe. The ~ 800-m-thick Ingeli lobe is comparable to the Insizwa lobe, in that it comprises a ~ 465-m-thick sequence of chromitiferous olivine-rich cumulates overlain by olivine-bearing gabbronoritic rocks that display chemical patterns characteristic of closed-system fractionation. The ultramafic cumulate rocks host relatively forsteritic (Fo_{86-80}) and Ni-rich olivine (1250-2450 ppm) as well as sparsely disseminated magmatic sulphide mineralisation along its upper margin. The ~ 50-m-thick Horseshoe lobe consists of ~ 40 m of sulphide-bearing olivine gabbronorite overlain by a thin layer of gabbro. The olivine gabbronorite hosts forsteritic (Fo_{81-78}) and Ni-poor (300-1000 ppm) olivine, comparable to that of the Tabankulu and Tonti lobes.

It is proposed that tholeiitic primary magmas concentrated in an upper crustal staging chamber hosted within Proterozoic basement rocks where they fractionated Mg-silicates and chromite, becoming comparable in composition to Lesotho-type basalts. Olivine- and chromite-bearing parent magmas upwelled via NW-SE-oriented structures and splayed at the level of the MAC, depositing chromitiferous olivine-rich cumulates within basal

depressions in the local metasedimentary country rocks. Prolonged magma flux instigated the assimilation of Sr-rich Proterozoic basement rocks, which triggered sulphide melt saturation. Parent magmas, now entraining relatively Ni-poor olivine and sulphide melt, intruded at the level of the MAC. This magma deposited sulphide-bearing olivine-rich cumulates, from which basal sulphide accumulations were formed. Lesotho-type basalt then flowed laterally over the olivine-rich cumulates which ultimately, underwent closed-system fractionation and deposited sparsely disseminated sulphides atop the olivine-rich cumulate pile. Basal depressions and feeder structures underlying the south-central portions of the MAC have the greatest potential for magmatic sulphide mineralisation.

Acknowledgements

Dr. Malcom Roberts and Siksha Bramdeo are thanked for their assistance during microprobe analysis at Rhodes University. Dr. Duncan Muir is thanked for their assistance during electron microanalysis at Cardiff University. Falconbridge Ventures of Africa and in particular, Andrew Pedley, are acknowledged for their financial support and assistance during sampling. B. Albrechtsen acknowledges financial support provided by CERMOD. Stephen Barnes and Judith Kinnaird are thanked for their constructive reviews that helped improve the manuscript. Hannah Hughes and Sisir Mondal are thanked for their editorial handling of this contribution.

References

Albrechtsen, B.H. 2006. *A Geochemical and Field Study of the Ingeli and Horseshoe Lobes, Mount Ayliff Complex, South Africa, and Its Potential for Magmatic Suphide Ores*. Rhodes University MSc Thesis.

Ashwal, L.D., Ziegler, A., Glynn, S., Truebody, T. and Bolhar, R. 2021. Sr-enriched glassy picrites from the Karoo Large Igneous Province are evolved, not primitive magmatic rocks. *Geochemistry, Geophysics, Geosystems*, **22**, e2020GC009561.

Bailie, R., Macey, P.H., Nethenzheni, S., Frei, D. and le Roux, P. 2017. The Keimoes Suite redefined: The geochronological and geochemical characteristics of the ferroan granites of the eastern Namaqua Sector, Mesoproterozoic Namaqua-Natal Metamorphic Province, southern Africa. *Journal of African Earth Sciences*, **134**, 737–765.

Barnes, S.J., Yao, Z.S., Mao, Y.J., Jesus, A.P., Yang, S., Taranovic, V. and Maier, W.D., 2023. Nickel in olivine as an exploration indicator for magmatic Ni-Cu sulfide deposits: A data review and re-evaluation. American Mineralogist, 108(1), pp.1-17.

Barnes, S.J. 2023. Lithogeochemistry in exploration for intrusion-hosted magmatic Ni–Cu–Co deposits. Geochemistry: Exploration, Environment, Analysis, 23(1), geochem2022-025.

Barnes, S.J., Godel, B., Gürer, D., Brenan, J.M., Robertson, J. and Paterson, D., 2013. Sulfide-olivine Fe-Ni exchange and the origin of anomalously Ni rich magmatic sulfides. Economic Geology, 108(8), pp.1971-1982.

Barnes, S.J., 1986. The effect of trapped liquid crystallisation on cumulus mineral compositions in layered intrusions. Contributions to Mineralogy and Petrology, 93(4), pp.524-531.

Barnes, S.-J. and Mansur, E.T. 2022. Distribution of Te, As, Bi, Sb, and Se in Mid-Ocean Ridge Basalt and Komatiites and in Picrites and Basalts from Large Igneous Provinces: Implications for the Formation of Magmatic Ni-Cu-Platinum Group Element Deposits. *Economic Geology*.

Beattie, P., Ford, C. and Russell, D., 1991. Partition coefficients for olivine-melt and orthopyroxene-melt systems. Contributions to Mineralogy and Petrology, 109(2), pp.212-224.

Bédard, J.H., 2014. Parameterizations of calcic clinopyroxene—Melt trace element partition coefficients. Geochemistry, Geophysics, Geosystems, 15(2), pp.303-336.

Bristow, J. W., Allsopp, H. L., Erlank, A. J., Marsh, J. S., & Armstrong, R. A. 1984. Strontium isotope characterisation of Karoo volcanic rocks. Petrogenesis of the Volcanic Rocks of the Karoo Province: *Geological Society of South Africa Special Publication*, 13, 295-329.

Bristow, J.W. and Cox, K.G. 1984. Volcanic rocks of the Lebombo-Nuanetsi-Sabi zone: classification and nomenclature. *In*: *Petrogenesis of the Volcanic Rocks of the Karoo Province, Special Publications, Vol. 13, Geological Society of South Africa*. 69–75.

Bruynzeel, D. 1957. *A Petrographic Study of the Waterfall Gorge Profile at Insizwa*.

Brzozowski, M., Hollings, P., Heggie, G., MacTavish, A., Wilton, D. and Evans-Lamswood, D., 2023. Characterizing the supra-and subsolidus processes that generated the Current PGE–Cu–Ni deposit, Thunder Bay North Intrusive Complex, Canada: insights from trace elements and multiple S isotopes of sulphides. Mineralium Deposita, pp.1-23.

Cawthorn, R.G. 1980. High-MgO Karroo Tholeiite and the formation of nickel-copper sulphide mineralisation in the Insizwa Intrusion, Transkei. *South African Journal of Science*, **76**, 467–471.

Cawthorn, R.G., Maske, S.I., De Wet, M.I., Groves, D.I., & Cassidy, K.F. (1988). Contrasting magma-types in the Mount Ayliff Intrusion (Insizwa Complex), Transkei; evidence from ilmenite compositions. The Canadian Mineralogist, 26(1), 145-160.

Cawthorn, R.G., Sander, B.K. and Jones, I.M., 1992. Evidence for the trapped liquid shift effect in the Mount Ayliff Intrusion, South Africa. *Contributions to Mineralogy and Petrology*, 111, pp.194-202.

Cawthorn, R.G. and Biggar, G.M. 1993. Crystallisation of titaniferous chromite, magnesian ilmenite and armalcolite in tholeiitic suites in the Karoo Igneous Province. *Contributions to Mineralogy and Petrology*, **114**, 221–235.

Cawthorn, R.G. and Kruger, F.J. 2004. Petrology and Ni–Cu–PGE potential of the Insizwa Lobe, Mount Ayliff Intrusion, South Africa. *The Canadian Mineralogist*, **42**, 303–324.

Cawthorn, R.G., De Wet, M., Maske, S., Groves, D.I. and Cassidy, K.F. 1986. Nickel sulphide potential of the Mount Ayliff intrusion (Insizwa complex), Transkei. *South African journal of science*, **82**, 572–576.

Cawthorn, R.G., Sander, B.K. and Jones, I.M. 1992. Evidence for the trapped liquid shift effect in the Mount Ayliff Intrusion, South Africa. *Contributions to Mineralogy and Petrology*, **111**, 194–202.

Chai, G. and Naldrett, A.J. 1992. The Jinchuan ultramafic intrusion: cumulate of a high-Mg basaltic magma. *Journal of Petrology*, **33**, 277–303.

Coetzee, A. and Kisters, A.F.M. 2020. Spatial variations of sills and implications for magma dispersal across the Karoo basin. *South African Journal of Geology*, **123**, 511–530.

De Decker, R. 1981. Geology of the Kokstad area (sheet 3028). *Geological survey, Government Printer, Pretoria*.

Dowsett NT**, J.& R. 1967. An exploration programme for nickel and copper in the differentiated intrusives of East Griqualand and Pondoland. *South African Journal of Geology*, **70**, 67–79.

Du Toit, A.L. 1910. Report on the Cu-Ni deposits of the Insizwa intrusion, Mount Ayliff, East Griqualand. *Fifteenth Annual Report, Cape of Good Hope Geological Commission, Department of Mines, Cape Town, South Africa*.

Duncan, A.R., Erlank, A.J. and Marsh, J.S. 1984. Regional geochemistry of the Karoo igneous province. *In*: *Petrogenesis of the Volcanic Rocks of the Karoo Province*. 355–388.

Eales, H. V. 1990. The Birds River intrusion-a quantitative model for Karoo Central Province basalt fractionation. *South African Journal of Geology*, **93**, 717–728.

Eales, H.V. and Marsh, J.S. 1979. High-Mg tholeiitic rocks and their significance in the Karoo central province. *South African Journal of Science*, **75**, 400.

Eales, H.V., Marsh, J.S. and Cox, K.G. 1984. *The Karoo Igneous Province: An Introduction*.

Eglington, B.M. and Armstrong, R.A. 2003. Geochronological and isotopic constraints on the Mesoproterozoic Namaqua–Natal Belt: evidence from deep borehole intersections in South Africa. *Precambrian Research*, **125**, 179–189.

Eglington, B.M., Harmer, R.E. and Kerr, A. 1986. Petrographic, Rb-Sr isotope and geochemical characteristics of intrusive granitoids from the Port Edward-Port Shepstone area, Natal. *South African Journal of Geology*, **89**, 199–213.

Ferré, E.C., Bordarier, C. and Marsh, J.S. 2002. Magma flow inferred from AMS fabrics in a layered mafic sill, Insizwa, South Africa. *Tectonophysics*, **354**, 1–23, https://doi.org/10.1016/S0040-1951(02)00273-1.

Gauert, C.D.K., De Waal, S.A. and Wallmach, T. 1995. Geology of the ultrabasic to basic Uitkomst complex, eastern Transvaal, South Africa: an overview. *Journal of African Earth Sciences*, **21**, 553–570, https://doi.org/10.1016/0899-5362(95)00112-3.

Ghiorso, M.S. and Sack, R.O. 1995. Chemical mass transfer in magmatic processes IV. A revised and internally consistent thermodynamic model for the interpolation and extrapolation of liquid-solid equilibria in magmatic systems at elevated temperatures and pressures. *Contributions to Mineralogy and Petrology*, **119**, 197–212.

Hasterok, D. and Chapman, D.S. 2011. Heat production and geotherms for the continental lithosphere. *Earth and Planetary Science Letters*, **307**, 59–70.

Heinonen, J.S., Jennings, E.S. and Riley, T.R. 2015. Crystallisation temperatures of the most Mg-rich magmas of the Karoo LIP on the basis of Al-in-olivine thermometry. *Chemical Geology*, **411**, 26–35.

Herzberg, C. and Asimow, P.D. 2015. PRIMELT 3 MEGA. XLSM software for primary magma calculation: peridotite primary magma MgO contents from the liquidus to the solidus. *Geochemistry, Geophysics, Geosystems*, **16**, 563–578.

Hughes, H.S.R., McDonald, I., Boyce, A.J., Holwell, D.A. and Kerr, A.C. 2016. Sulphide Sinking in Magma Conduits: Evidence from Mafic–Ultramafic Plugs on Rum and the Wider North Atlantic Igneous Province. *Journal of Petrology*, **57**, 383–416.

Iacono-Marziano, G., Le Vaillant, M., Godel, B. M., Barnes, S. J., & Arbaret, L. 2022. The critical role of magma degassing in sulphide melt mobility and metal enrichment. Nature communications, 13(1), 1-10.

Jensen, M.L. 1967. Sulphur isotopes and mineral genesis. *Geochemistry of hydrothermal ore deposits*, 143–165.

Jones, M.Q.W. and Scheiber-Enslin, S.E. 2022. Heat flow in the Main Karoo Basin, South Africa. *South African Journal of Geology 2022*, **125**, 345–360.

Jourdan, F., Féraud, G., Bertrand, H., Kampunzu, A.B., Tshoso, G., Watkeys, M.K. and Le Gall, B. 2005. Karoo large igneous province: Brevity, origin, and relation to mass extinction questioned by new 40Ar/39Ar age data. *Geology*, **33**, 745–748.

Li, C. and Naldrett, A.J., 1999. Geology and petrology of the Voisey's Bay intrusion: reaction of olivine with sulphide and silicate liquids. *Lithos*, 47(1-2), pp.1-31.

Li, C., Lightfoot, P.C., Amelin, Y., & Naldrett, A.J. 2000. Contrasting petrological and geochemical relationships in the Voisey's Bay and Mushuau intrusions, Labrador, Canada: implications for ore genesis. *Economic geology*, **95**(4), 771-799.

Lightfoot, P.C. and Naldrett, A.J. 1983. The geology of the Tabankulu Section of the Insizwa Complex. *Transactions of the Geological Society of South Africa*, **86**, 169–187.

Lightfoot, P.C. and Naldrett, A.J. 1984. Chemical variation in the Insizwa complex, Transkei, and the nature of the parent magma. *The Canadian Mineralogist*, **22**, 111–123.

Lightfoot, P.C., Naldrett, A.J. and Hawkesworth, C.J. 1984. The geology and geochemistry of the Waterfall Gorge section of the Insizwa Complex with particular reference to the origin of the nickel sulphide deposits. *Economic Geology*, **79**, 1857–1879.

Lightfoot, P.C., Naldrett, A.J. and Hawkesworth, C.J. 1987. Re-evaluation of chemical variation in the Insizwa Complex, Transkei. *The Canadian Mineralogist*, **25**, 79–90.

Maier, W.D., Barnes, S.J. and Marsh, J.S. 2001. PGE in southern African flood basalts: implications for magmatic sulphide exploration. *In*: *Mineral Deposits at the Beginning of the 21st Century*. 665–668.

Maier, W.D., Marsh, J.S., Barnes, S.-J. and Dodd, D.C. 2002. The distribution of platinum group elements in the Insizwa lobe, Mount Ayliff Complex, South Africa: implications for Ni-Cu-PGE sulphide exploration in the Karoo igneous province. *Economic Geology*, **97**, 1293–1306.

Maier, W.D., Prevec, S.A., Scoates, J.S., Wall, C.J., Barnes, S.-J. and Gomwe, T. 2018. The Uitkomst intrusion and Nkomati Ni-Cu-Cr-PGE deposit, South Africa: trace element geochemistry, Nd isotopes and high-precision geochronology. *Mineralium Deposita*, **53**, 67–88.

Mao, Y. J., Barnes, S. J., Duan, J., Qin, K. Z., Godel, B. M., & Jiao, J. 2018. Morphology and particle size distribution of olivines and sulphides in the Jinchuan Ni–Cu sulphide deposit: evidence for sulphide percolation in a crystal mush. *Journal of Petrology*, 59(9), 1701-1730.

Marsh, J.S. 2004. Rare earth element geochemistry of the 29malfi29 lobe of the Mount Ayliff Complex, Eastern Cape, South Africa. *South African journal of science*, **100**, 556–560.

Marsh, J.S., Allen, P. and Fenner, N. 2003. The geochemical structure of the Insizwa lobe of the Mount Ayliff Complex with implications for the emplacement and evolution of the complex and its Ni-sulphide potential. *South African Journal of Geology*, **106**, 409–428.

Marsh, J.S., Hooper, P.R., Rehacek, J., Duncan, R.A., Duncan, A.R., Mahoney, J.J. and Coffin, M.F. 1997. Stratigraphy and age of Karoo basalts of Lesotho and implications for correlations within the Karoo igneous province. *Geophysical Monograph-American Geophysical Union*, **100**, 247–272.

Maske, S. 1964. The petrography of the Ingeli mountain range. Stellenbosch University PhD Thesis.

Maske, S. and Cawthorn, R.G. 1986. The nickel occurrence in the Insizwa Complex, Transkei. *In*: *Mineral Deposits of Southern Africa*. 2149–2158.

Matzen, A.K., Baker, M.B., Beckett, J.R., Wood, B.J. and Stolper, E.M. 2017. The effect of liquid composition on the partitioning of Ni between olivine and silicate melt. *Contributions to Mineralogy and Petrology*, **172**, 1–18.

Mavrogenes, J.A. and O'Neill, H.C. 1999. The relative effects of pressure, temperature and oxygen fugacity on the solubility of sulphide in mafic magmas. *Geochimica et Cosmochimica Acta*, **63**, 1173–1180.

McDonough, W.F. and Sun, S.S. 1995. The composition of the Earth. *Chemical Geology*, **120**, 223–253.

Métrich, N., & Wallace, P. J. 2008. Volatile abundances in basaltic magmas and their degassing paths tracked by melt inclusions. Reviews in mineralogy and geochemistry, 69(1), 363-402.

Mungall, J.E. and Su, S. 2005. Interfacial tension between magmatic sulphide and silicate liquids: Constraints on kinetics of sulphide liquation and sulphide migration through silicate rocks. *Earth and Planetary Science Letters*, **234**, 135–149.

Mungall, J. E., Harvey, J. D., Balch, S. J., Azar, B., Atkinson, J., & Hamilton, M. A. (2010). Eagle's nest: A magmatic Ni-sulphide deposit in the James Bay Lowlands, Ontario, Canada.

Naldrett, A.J., Wilson, A.H., Kinnaird, J.A. and Chunnett, G. 2009. PGE Tenor and Metal Ratios within and below the Merensky Reef , Bushveld Complex : Implications for its Genesis. *American Mineralogist*, **50**, 473–506.

Nethenzheni, S.S. 2016. *The Geochemistry, Geochronology and Petrogenetic Characteristics of Two Granitic Suites on the Eastern Margin of the Namaqua Sector, Namaqua-Natal Mobile Belt, South Africa*.

Neumann, E.-R., Svensen, H., Galerne, C.Y. and Planke, S. 2011. Multistage evolution of dolerites in the Karoo large igneous province, Central South Africa. *Journal of Petrology*, **52**, 959–984.

Poldervaart, A. and Walker, F. 1943. The petrology of the elephant's head dike and the new 30malfi sheet (matatiele). *Transactions of the Royal Society of South Africa*, **30**, 85–119, https://doi.org/10.1080/00359194309519833.

Poldervaart, A. and Walker, F. 1943. The petrology of the Elephant's Head dike and the New Amalfi sheet (Matatiele). *Transactions of the Royal Society of South Africa*, **30**, 85–119.

Poldervaart, A. and Walker, F. 1946. The petrology of the Mount Arthur dolerite complex, East Griqualand. *Transactions of the Royal Society of South Africa*, **31**, 83–110.

Ripley, E.M. and Li, C. 2013. Sulphide Saturation in Mafic Magmas: Is External Sulphur Required for Magmatic Ni-Cu-(PGE) Ore Genesis? *Economic Geology*, **108**, 45–58.

Robertson, J.C., Barnes, S.J. and Le Vaillant, M., 2015. Dynamics of magmatic sulphide droplets during transport in silicate melts and implications for magmatic sulphide ore formation. Journal of Petrology, 56(12), pp.2445-2472.

Roeder, P.L. and Emslie, R.F. l. 1970. Olivine-liquid equilibrium. *Contributions to mineralogy and petrology*, **29**, 275–289.

Sander, B.K. and Cawthorn, R.G. 1995. Laminated olivine spinifex textures in the Mount Ayliff intrusion, South Africa. *Mineralogy and Petrology*, **54**, 1–10.

Sander, B.K. and Cawthorn, R.G. 1996. 2.5-D gravity model of the Ni-Cu-PGM mineralized Mount Ayliff Intrusion (Insizwa Complex), South Africa. *Journal of applied geophysics*, **35**, 27–43.

Scholtz, D.L. 1937. The magmatic nickeliferous ore deposits of East Griqualand and Pondoland. *South African Journal of Geology*, **40**, 81–210.

Smith, W.D., Maier, W.D. and Bliss, I. 2021. The geology, geochemistry, and petrogenesis of the Huckleberry Cu-Ni-PGE prospect in the Labrador Trough, Canada: Perspectives for regional prospectivity. *Ore Geology Reviews*, **128**, 103905.

Smith, W.D., Maier, W.D., Barnes, S.J., Moorhead, G., Reid, D. and Karykowski, B.T. 2021. Element mapping the Merensky Reef of the Bushveld Complex. *Geoscience Frontiers*, **12**, 101101.

Smythe, D.J., Wood, B.J. and Kiseeva, E.S. 2017. The S content of silicate melts at sulphide saturation: new experiments and a model incorporating the effects of sulphide composition. *American Mineralogist*, **102**, 795–803.

Tischler, S.E., Cawthorn, R.G., Kingston, G.A. and Maske, S. 1981. Magmatic Cu-Ni-PGE mineralisation at Waterfall Gorge, Insizwa, Pondoland, Transkei. *The Canadian Mineralogist*, **19**, 607–618.

Wallace, P., & Carmichael, I. S. 1992. Sulphur in basaltic magmas. Geochimica et Cosmochimica Acta, 56(5), 1863-1874.

Williams, C.M. 1995. *Petrogenesis of the New Amalfi Sheet a Highly Differentiated Karoo Intrusion*.

Yao, Z., Qin, K. and Mungall, J.E., 2018. Tectonic controls on Ni and Cu contents of primary mantle-derived magmas for the formation of magmatic sulfide deposits. American Mineralogist, 103(10), pp.1545-1567.

Figure Captions

Figure 1. Summary of the Mount Ayliff Complex (MAC). **A.** Map and location of the MAC showing the areal extent of the five lobes (after Maier *et al.* 2002) and locations of the Taylor's Koppie Dyke (Maier *et al*. 2002) and Tabankulu feeder (Lightfoot and Naldrett 1983). **B.** Generalised stratigraphic columns reported across the MAC, ordered from approximately north to south. Note the appearance of troctolite at Tabankulu that has also been reported at Ingeli. **C-D.** Geological maps of the Ingeli and Horseshoe lobes showing the traverse of samples used in the present study. Note the spatial association with Karoo dolerites.

Figure 2. Summary of the lower ultramafic portion of the Ingeli lobe. **A-B.** Photomicrographs of the Ingeli *basal olivine gabbronorite* (IT-7). Note the occurrence of chromite and melt inclusions within olivine grains. **C.** Chromite chain inclusions within olivine in the Ingeli *lherzolite unit* (sample IT-13). **D.** Photomicrograph of the upper Ingeli *lherzolite unit* (IT-21) showing the occurrence of olivine clusters within an orthopyroxene oikocryst. **E.** Mg-Cr-log[K]-S element map highlighting the distribution of sulphide, chromite, and phlogopite in the upper portion of Ingeli *lherzolite unit* (IT-21). **F-G.** Mg-Al-S-K-Cr-P-Ti element maps of olivine-hosted melt inclusions. Note the occurrence of sulphide and chromite (IT-21). **H.** Reflected light photomicrograph of a sulphide bleb amongst chromite in the upper Ingeli *lherzolite unit.* Abbreviations: ol = olivine, pl = plagioclase, (c) = cumulus, (i) = intercumulus, opx = orthopyroxene, cpx = clinopyroxene, chr = chromite, phl = phlogopite, ap = apatite, ilm = ilmenite, sul = sulphide, po = pyrrhotite, pn = pentlandite, ccp = chalcopyrite.

Figure 3. Summary of the upper mafic portion of the Ingeli lobe. **A-B**. Photomicrographs of the Ingeli *central gabbronorite* (IT-23 and IT-25) showing subophitic texture, intercumulus clinopyroxene, and undeformed plagioclase grains with no preferred orientation. **C.** Photomicrograph of the Ingeli *upper olivine gabbronorite* (IT-31) showing the occurrence of anhedral olivine grains with melt inclusions. **D.** Photomicrograph of the Ingeli *upper gabbronorite* showing intercumulus pyroxenes, including inverted pigeonite (i. pgt).

Figure 4. Stratigraphic geochemical variation in the Ingeli lobe. **A-E.** Traverse CIPW normative mineralogy, whole-rock geochemistry, and mineral chemistry of the Ingeli lobe. Note the upward increase in MgO, Cr, Fo_{ol}, and Mg_{px} in the *basal olivine gabbronorite,* the mostly constant composition of the *lherzolite unit*, and the increase in chalcophile metals at the ultramafic-mafic transition (~ 450 m).

Figure 5. Summary of the Horseshoe lobe units. **A-B.** Photomicrographs of the *olivine gabbronorite*. Note the occurrence of chromite and olivine-hosted melt inclusions (HS15 and

HS-24). **C.** Mg-Ca-Cr-S-K-log[K] element map of the *olivine gabbronorite* (HS-14). **D.** Mg-Ca-log[K]-S-P element map of an olivine-hosted melt inclusions that contains sulphides. **E.** Photomicrography of the upper portion of the *olivine gabbronorite* illustrating the relative upward increase in the proportion of cumulus plagioclase. **F.** Reflected light photomicrograph of blebby sulphides in the *olivine gabbronorite* (HS-15). **G.** Photomicrograph of the Horseshoe *upper gabbro* showing alteration of intercumulus pyroxenes and randomly oriented needle-like plagioclase grains (HS-08).

Figure 6. Stratigraphic geochemical variation in the Horseshoe lobe. **A-E.** Traverse CIPW normative mineralogy, whole-rock geochemistry, and mineral chemistry of the Horseshoe lobe. Note the constant composition of the *olivine gabbronorite* with a subtle basal reversal and the higher S contents relative to the Ingeli lobe ultramafic units.

Figure 7. Whole-rock geochemistry for the MAC units and local parent magma analogues. **A-F.** MgO *versus* SiO_2, TiO_2, Al_2O_3, FeOt, CaO, and Na_2O+K_2O for rock units of the Ingeli and Horseshoe lobes. Note the compositional 'gap' between the lower ultramafic rock types and the upper mafic rock types. Samples from the Insizwa lobe (Maier *et al.* 2002; Marsh *et al.* 2003), Ecca Group metasedimentary country rocks (Neumann *et al.* 2011), and Proterozoic basement rocks (Bailie *et al.* 2017) have been underlain. Possible parent magma analogues have been overlain, including the Waterfall Gorge Sill (Cawthorn and Kruger 2004), the Insizwa footwall sill (Maier *et al.* 2002), the Insizwa chilled margin (Marsh *et al.* 2002), Taylor's Koppie Dyke (Marsh *et al.* 2002), and Lesotho-type basalt (Marsh *et al.* 1997).

Figure 8. Binary geochemical diagrams for the MAC units and local parent magma analogues. **A-B.** Mg# (mol.%) *versus* Al2O3 (wt.%) and Al2O3/TiO2 cumulate discrimination diagrams of Barnes (2023). Note that the uppermost Ingeli *upper olivine gabbronorite* and Horseshoe *upper gabbro* are the only studied units consistent with mafic non-cumulates. **C-D.** Mg# (mol.%) *versus* Cr/V and Ni. Note the relatively low Ni content of the Horseshoe *olivine gabbronorite* compared with that of Ingeli and the variable Ni concentrations of the Insizwa chilled margin.

Figure 9. Primitive mantle-normalised (McDonough and Sun 1995) multi-element plots for the Ingeli rock units underlain by the trace element concentrations of Lesotho-type basalts (Marsh *et al.* 1997), the Insizwa chilled margin (Marsh *et al.* 2004), Ecca Group metasedimentary country rocks (Neumann *et al.* 2011), and Proterozoic basement rocks (Bailie *et al.* 2017). Note the elevated Sr and Eu concentrations of the gabbronoritic units and the comparable profiles between Lesotho-type basalt and the Insizwa chilled margin.

Figure 10. Binary diagrams of chalcophile elements for the MAC units and local parent magma analogues. **A-B.** S *versus* Ni and Cu for the full dataset. Note the strong positive correlations between S and chalcophile metals in the Horseshoe rocks and in Taylor's Koppie Dyke. **C.** Ni *versus* Cu. Note the subdivision of non-mineralised olivine-bearing cumulates (Ni/Cu > 10) from mineralised olivine-bearing cumulates (Ni/Cu ~ 5-10). **D.** Cu *versus* Zr, whereby only Ingeli's lherzolite unit and Horseshoe's olivine gabbronorite show moderate sulphide accumulation, together with the Insizwa lobe rocks and some Taylor's Koppie Dyke samples.

Figure 11. Summary of historic Sr-isotopic data for the MAC and local rock units. **A.** Histogram of $^{87}Sr/^{87}Sr_{(i)}$ at 183 Ma for the Insizwa rock units, Karoo dolerites, country rocks, Proterozoic basement rocks, and the Waterfall Gorge Sills. **B.** Histogram of $^{87}Sr/^{87}Sr_{(i)}$ at 183 Ma for rock units related to the Insizwa lobe. Note the isotopic difference between the lower ultramafic and upper mafic portions of the Insizwa lobe, whereby Karoo dolerite isotopic compositions align with that of the upper mafic rocks of the Insizwa lobe. Data collated from Lightfoot and Naldrett (1984), Eglington *et al.* (1983), Marsh *et al.* (1997), Maier *et al.* (2002), Cawthorn and Kruger (2004), Jourdan *et al.* (2007), Neumann *et al.* (2011), and Bailie *et al.* (2017).

Figure 12. Parent magma composition approximation using the method of Chai and Naldrett (1992) and Li *et al.* (2000). **A.** Ingeli major element and olivine data predict a relatively high-MgO parent magma, though note the poor correlation between MgO and FeOt. **B.** Horseshoe major element (corrected for cumulus plagioclase) and olivine data predict a relatively low-MgO parent magma.

Figure 13. Summary of the modelled whole-rock geochemical signatures. **A-D.** MgO *versus* TiO_2, Al_2O_3, Fe_2O_3t, and CaO showing the results of alphaMELTS modelling (Table 6) superimposed on the full dataset. The red line corresponds to the composition of the QU1-1-9 dolerite liquid during assimilation-batch crystallisation of Proterozoic basement rock at 1 kbar (red star to yellow star) and then fractional crystallisation at 200 bars (yellow star onwards). The *Basal Zone* units of the MAC can be explained as variable proportions of olivine-spinel cumulates and contaminated doleritic liquid, while the *Central Zone* gabbronoritic units can be explain as mixtures of plagioclase-clinopyroxene cumulates and fractionated doleritic liquid.

Figure 14. Primitive mantle-normalised multi-element plots showing the results of alphaMELTS modelling (Table 6) superimposed on the average Proterozoic basement rock (Bailie *et al.* 2017) and Lesotho-type basalts (Marsh *et al.* 1997). **A.** Measured and modelled Ingeli *central gabbronorite* composition and its corresponding liquid composition. **B.**

Measured and modelled compositions of the Ingeli *Basal Zone* units and the corresponding liquid composition of the modelled *Lherzolite unit*. **C.** Measured and modelled compositions of the Horseshoe *olivine gabbronorite* and its corresponding liquid composition as well as the measured and modelled composition of the Insizwa *chilled margin* (Marsh *et al.* 2003).

Figure 15. $^{87}Sr/^{87}Sr_{(i)}$ at 183 Ma *versus* 100/Sr for the measured and modelled data. **A.** $^{87}Sr/^{87}Sr_{(i)}$ and 100/Sr values of the collated dataset (Fig. 11). The composition of bulk Earth is given as $^{87}Sr/^{87}Sr_{(i)}$ of 0.7045 and an Sr of 320 ppm. The $^{87}Sr/^{87}Sr_{(i)}$ and 100/Sr values of the modelled whole-rock and plagioclase compositions for the Ingeli *central gabbronorite* and *basal olivine gabbronorite* are overlain. **B.** Enhanced portion of the diagram showing binary mixing curves between unevolved QU1-1-9 dolerite and possible contaminants. The composition of the QU1-1-9 dolerite liquid as it undergoes assimilation-batch crystallisation at 1 kbar is overlain.

Figure 16. Summary of measured and modelled olivine compositional data. **A.** Map of the MAC (see Fig. 1) with annotated Fo (mol.%) versus Ni (ppm) diagrams highlighting the occurrence of Ni-poor olivine in the south-central portion. **B.** The entire olivine dataset overlain on 50th and 90th percentile contours of olivine from 'barren' intrusions associated with large igneous provinces (Barnes *et al.* 2023). A field of olivine compositions modelled from fractional crystallisation of mantle-derived basaltic magmas is also presented (Yao *et al.* 2018). Note that olivine from the *Basal Zones* of Tabankulu, Tonti, and Horseshoe are particularly Ni-poor. **C.** MAC olivine clustered by *k*-means into three groups and underlain by 50th and 90th percentile contours. The pink star represents olivine in equilibrium with the uncontaminated QU1-1-9 dolerite (Table 5) and the red line is the result of batch crystallization at 1 kbar. The blue and pink lines represent olivine compositions undergoing batch crystallization in the presence of different proportions of sulphide melt (Barnes *et al.* 2023). The black line represents the effect of closed-system batch equilibration between olivine and sulphide melt as a function of *R*-factor (Barnes *et al.* 2013). The grey line represents the back-fractionation of uncontaminated QU1-1-9 dolerite using PRIMELT (Herzberg and Asimow 2015). The grey arrows represent the theoretical effect of trapped liquid shift (Barnes *et al.* 2023). 1 = Marsh *et al.* (2003); 2 = Cawthorn *et al.* (1992); 3 = Lightfoot and Naldrett (1984); 4 = Cawthorn *et al.* (2004); 5 = Lightfoot and Naldrett (1983); 6 = Barnes *et a.* (2023); 7 = Yao *et al.* (2018); 8 = Williams (1995).

Figure 17. A-C. Petrogenetic model for the MAC (modified from Lightfoot and Naldrett 1983). The reader is referred to the text for a detailed explanation.

Table Captions

Table 1. Summary of mineral compositions in the Ingeli lobe.

Table 2. Summary of mineral compositions in the Horseshoe lobe.

Table 3. Representative XRF whole-rock geochemical analyses of the Ingeli and Horseshoe units. The full dataset is reported in the supplementary materials.

Table 4. ICP-MS trace element (ppm) concentrations of the Ingeli units.

Table 5. Compositions used in alphaMELTS modelling.

Table 6. Comparison between measured and modelled compositions of MAC cumulate rocks.

[1]Rock:		LU				BOG				COG and CG				UOG and UG			
Statistic:		$\bar{x}$	2σ	Min	Max	$\bar{x}$	2σ	Min	Max	$\bar{x}$	2σ	Min	Max	$\bar{x}$	2σ	Min	Max
OLIVINE		*n = 39*				*n* = 33				*n = 6*				*n* = 14			
wt.%	SiO_2	39.8	0.98	38.7	40.1	39.5	1.28	39.1	40.8	36.8	0.33	36.7	37.0	35.8	0.69	35.3	36.2
wt.%	FeO	15.1	2.43	14.2	17.4	15.5	1.88	13.9	16.6	30.7	0.89	30.4	31.0	33.8	3.43	32.0	35.6
wt.%	MgO	44.3	3.35	41.3	45.7	43.9	2.29	42.7	46.3	31.5	0.37	31.4	31.7	28.9	2.33	27.3	30.1
wt.%	CaO	0.07	0.04	0.04	0.10	0.06	0.03	0.05	0.10	0.06	0.03	0.05	0.07	0.08	0.04	0.05	0.10
wt.%	Total	99.8	1.81	98.0	100.8	99.5	1.56	98.9	101.0	99.6	1.61	99.1	100.2	99.1	0.97	98.5	99.8
ppm	Ni	1810	733	1500	2400	1900	715	1300	2400	750	424	600	900	1060	415	800	1300
mol.%	Fo	83.9	3.16	80.8	85.1	83.4	2.31	82.2	85.5	64.7	0.28	64.6	64.8	60.4	4.34	57.7	62.7
ORTHOPYROXENE		*n = 21*				*n* = 27				*n = 24*				*n = 22*			
wt.%	SiO_2	55.8	1.15	54.9	56.8	55.7	0.98	55.2	56.4	54.5	1.72	53.1	55.6	52.5	1.71	51.2	53.5
wt.%	Al_2O_3	1.3	0.39	1.2	1.7	1.4	0.31	1.1	1.5	1.0	0.49	0.7	1.5	0.7	0.29	0.5	0.9
wt.%	TiO_2	0.3	0.11	0.3	0.4	0.4	0.40	0.2	0.8	0.3	0.28	0.1	0.5	0.4	0.17	0.3	0.5
wt.%	Cr_2O_3	0.5	0.21	0.4	0.7	0.5	0.17	0.3	0.6	0.2	0.32	0.0	0.5	0.1	0.09	0.0	0.1
wt.%	FeO	9.4	1.97	7.4	10.3	9.4	1.30	8.7	10.6	15.9	4.52	13.1	18.6	21.6	5.29	18.6	26.2
wt.%	MnO	0.2	0.07	0.2	0.3	0.2	0.11	0.2	0.3	0.4	0.11	0.3	0.4	0.4	0.09	0.4	0.5
wt.%	MgO	30.3	3.11	27.1	31.7	30.0	1.32	29.2	31.2	25.4	3.15	23.2	27.4	21.5	3.66	17.9	23.5
wt.%	CaO	2.0	4.52	1.7	8.4	2.8	0.52	1.6	2.3	2.1	0.70	1.4	2.5	1.8	0.84	1.0	2.3
wt.%	Na_2O	0.1	0.15	0.0	0.2	0.1	0.26	0.0	0.4	0.0	0.00	0.0	0.0	0.0	0.10	0.0	0.1
wt.%	Total	100.0	1.16	99.5	101.1	100.4	1.01	99.5	100.9	99.6	1.42	98.4	100.7	99.0	1.14	98.3	100.1
mol.%	Mg	85.1	2.42	83.6	86.7	85.1	2.24	83.3	86.5	74.0	7.85	69.0	78.8	64.0	9.55	54.9	69.2
CLINOPYROXENE		*n = 30*				*n* = 22				*n = 29*				*n* = 30			
wt.%	SiO_2	52.9	0.83	52.1	53.8	52.5	0.84	51.8	53.4	52.9	1.04	50.6	53.6	51.7	1.74	53.0	53.6
wt.%	Al_2O_3	2.38	0.43	2.23	2.62	2.49	0.20	1.31	1.96	1.59	0.40	1.19	2.07	1.70	0.53	2.80	2.07
wt.%	TiO_2	0.47	0.23	0.32	0.73	0.51	0.25	0.38	0.78	0.54	0.26	0.40	0.66	0.54	0.20	0.70	0.66
wt.%	Cr_2O_3	1.04	1.06	0.99	1.14	1.28	0.08	0.12	0.79	0.34	0.41	0.10	0.72	0.33	0.38	2.31	0.72
wt.%	FeO	5.2	1.22	4.8	5.4	4.9	0.50	7.9	10.5	9.4	1.86	8.7	13.3	10.7	3.25	5.7	13.3
wt.%	MnO	0.15	0.07	0.10	0.19	0.14	0.05	0.19	0.29	0.25	0.06	0.20	0.31	0.25	0.08	0.19	0.31
wt.%	MgO	17.9	2.14	16.8	19.0	17.6	1.16	15.6	18.5	16.5	2.07	14.0	15.6	14.7	1.26	19.1	15.6
wt.%	CaO	19.3	1.78	18.2	21.1	19.7	1.66	15.8	19.5	18.1	2.55	18.0	19.6	18.9	1.02	21.1	19.6
wt.%	Na_2O	0.35	0.12	0.31	0.39	0.42	0.06	0.15	0.24	0.20	0.06	0.23	0.29	0.27	0.04	0.53	0.29
wt.%	Total	99.6	1.81	98.5	100.7	99.6	1.36	98.4	100.5	99.8	1.31	98.5	100.6	99.2	1.47	101.1	100.6
mol.%	Mg	86.1	3.43	85.5	86.9	86.6	1.09	73.2	80.7	75.8	4.77	65.8	76.0	71.1	7.66	89.1	76.0
PLAGIOCLASE		*n* = 36				*n* = 27				*n* = 30				*n* = 30			
wt.%	SiO_2	51.7	1.81	50.2	52.8	51.1	2.70	50.3	55.3	50.1	2.31	48.4	51.8	51.4	2.00	50.0	52.9
wt.%	Al_2O_3	31.1	1.00	30.5	32.0	31.1	2.33	28.2	32.3	32.2	1.88	31.0	33.7	30.9	1.55	29.8	31.9
wt.%	CaO	13.1	1.11	12.2	13.8	13.2	2.33	10.1	14.2	14.5	1.92	13.3	15.9	13.0	1.62	11.4	13.8
wt.%	Na_2O	3.9	0.62	3.6	4.5	3.9	1.26	3.5	5.6	3.1	1.00	2.4	3.8	3.9	0.56	3.5	4.3
wt.%	K_2O	0.3	0.06	0.25	0.34	0.3	0.11	0.21	0.40	0.2	0.10	0.16	0.30	0.3	0.07	0.25	0.38
wt.%	Total	100.3	1.20	98.8	100.5	99.8	1.49	99.4	101.8	100.5	0.68	99.8	100.9	99.8	1.54	99.1	100.9
mol.%	An	65.1	5.43	60.2	68.1	64.9	11.31	50.0	69.4	72.3	9.11	65.7	78.3	65.1	5.84	60.5	68.4

[1]BOG = basal olivine gabbronorite, LU = lherzolite unit, COG = central olivine gabbronorite, CG = central gabbronorite, UOG = upper olivine gabbronorite, UG = upper gabbronorite

Table 1

	[1]Rock:	**HSOG**							**HSG**
	Sample	HS-18	HS-15	HS-14	HS-13	HS-12	HS-11	HS-10	HS-8
					OLIVINE				
	Count:	4	4	4	4	4	3	4	
wt.%	SiO_2	38.8	39.1	38.9	39.0	39.0	39.2	39.3	
wt.%	FeO	21.2	19.1	19.0	18.3	18.6	18.8	18.1	
wt.%	MnO	0.29	0.28	0.27	0.24	0.29	0.29	0.27	
wt.%	MgO	39.8	41.5	41.7	41.7	40.8	41.8	42.2	
wt.%	CaO	0.12	0.17	0.16	0.15	0.14	0.17	0.14	
wt.%	Total	100.3	100.3	100.1	99.4	99.0	100.4	100.1	
ppm	Ni	900	800	800	600	600	300	600	
mol.%	Fo	77.0	79.4	79.7	80.3	79.6	79.8	80.7	
					ORTHOPYROXENE				
	Count:	1	4	3	3	1	2	1	3
wt.%	SiO_2	54.3	55.1	54.7	55.3	55.2	55.6	55.7	53.4
wt.%	Al_2O_3	1.5	1.2	1.7	1.3	1.3	0.9	1.0	1.4
wt.%	TiO_2	0.8	0.4	0.3	0.2	0.5	0.4	0.2	0.2
wt.%	Cr_2O_3	0.2	0.2	0.4	0.3	0.3	0.3	0.4	0.4
wt.%	FeO	13.6	11.9	10.3	10.3	11.1	11.0	10.4	16.2
wt.%	MnO	0.3	0.3	0.3	0.3	0.2	0.3	0.2	0.3
wt.%	MgO	27.6	28.9	29.1	29.5	28.6	29.6	29.7	23.2
wt.%	CaO	2.0	2.0	2.3	2.3	2.0	2.1	2.2	4.1
wt.%	Na_2O	0.1	0.0	0.0	0.0	0.0	0.0	0.0	0.1
wt.%	Total	100.4	100.1	99.0	99.5	99.2	100.2	99.9	99.3
mol.%	Mg	78.4	81.3	83.4	83.6	82.1	82.8	83.6	71.8
					CLINOPYROXENE				
	Count:		1	4	2	3	2	4	4
wt.%	SiO_2		51.9	52.4	53.0	53.5	53.1	53.0	52.4
wt.%	Al_2O_3		2.47	2.35	2.16	2.18	2.07	2.02	1.43
wt.%	TiO_2		0.71	0.54	0.31	0.28	0.51	0.47	0.49
wt.%	Cr_2O_3		0.62	0.59	0.65	0.58	0.94	0.89	0.11
wt.%	FeO		6.58	6.07	5.93	6.03	6.21	5.88	11.89
wt.%	MnO		0.21	0.22	0.22	0.22	0.18	0.16	0.28
wt.%	MgO		17.94	18.06	18.64	18.86	18.58	18.66	15.83
wt.%	CaO		18.25	18.47	17.88	17.26	17.99	18.38	17.13
wt.%	Na_2O		0.19	0.26	0.23	0.22	0.27	0.25	0.18
wt.%	Total		98.9	99.0	99.0	99.1	99.9	99.7	99.8
mol.%	Mg		82.9	84.1	84.9	84.8	84.2	85.0	70.4
					PLAGIOCLASE				
	Count:	4	4	4	4	4	3	4	4
wt.%	SiO_2	51.6	53.9	51.3	51.1	51.8	51.0	51.0	51.6
wt.%	Al_2O_3	30.2	29.3	30.3	30.8	30.0	31.0	30.5	30.2
wt.%	CaO	12.8	11.5	12.9	13.3	12.6	13.6	13.2	13.1
wt.%	Na_2O	3.81	4.64	3.79	3.51	3.79	3.61	3.69	4.13
wt.%	K_2O	0.27	0.35	0.28	0.24	0.26	0.23	0.25	0.23
wt.%	Total	99.2	100.0	99.3	99.3	98.7	99.7	98.9	99.8
mol.%	An	64.9	57.8	65.2	67.7	64.7	67.5	66.3	63.6

[1]HSOG = Horseshoe olivine gabbronorite, HSG = Horseshoe gabbro

Table 2

	Location:	Ingeli lobe							Horseshoe lobe		
	Sample:	IT-3	IT-7	IT-14	IT-22	1T-24	IT-30	IT-34	HS18	HS13	HS8
	Rock:	BOG	BOG	LU	COG	CG	UOG	UG	HSOG	HSOG	HSG
wt.%	SiO_2	38.3	42.0	41.4	43.2	50.9	50.0	50.6	48.3	43.0	54.1
wt.%	TiO_2	0.35	0.24	0.16	0.21	0.26	0.35	0.58	0.57	0.36	0.90
wt.%	Al_2O_3	5.39	4.00	2.85	16.2	18.4	17.6	15.3	8.74	5.93	15.4
wt.%	Fe_2O_3 t	15.2	14.1	13.8	9.85	5.41	8.13	9.97	13.3	15.1	10.9
wt.%	MnO	0.21	0.19	0.18	0.12	0.11	0.13	0.18	0.18	0.20	0.17
wt.%	MgO	32.3	35.1	37.8	18.2	8.09	8.37	8.25	22.0	28.2	6.92
wt.%	CaO	4.87	2.84	2.03	8.34	13.6	12.8	11.2	5.78	3.66	9.73
wt.%	Na_2O	0.57	<0.03	<0.03	0.87	1.38	1.94	2.06	0.88	0.31	2.16
wt.%	K_2O	0.37	0.23	0.16	0.21	0.19	0.28	0.29	0.48	0.30	0.80
wt.%	P_2O_5	0.05	0.04	0.03	0.04	0.03	0.04	0.07	0.11	0.09	0.15
wt.%	LOI	0.18	0.61	0.49	1.69	0.26	0.03	0.17	0.44	0.62	0.02
wt.%	Total	98.5	100.1	99.7	99.2	98.9	99.6	98.4	99.3	98.6	101.2
ppm	S	404	395	420	638	188	136	71	932	1530	840
ppm	Sc	15	11	13	<1	17	15	27	16	14	26
ppm	V	113	89	73	70	185	148	205	144	113	213
ppm	Cr	2872	3732	3427	1785	835	528	275	2504	2730	231
ppm	Co	127	135	145	84	28	45	56	98	125	52
ppm	Ni	1265	1376	1571	149	48	139	113	383	561	24
ppm	Cu	74	54	57	125	54	35	54	101	200	48
ppm	Zn	90	85	77	51	34	51	63	85	89	88
ppm	Ga	14	13	12	18	23	22	22	17	14	24
ppm	Sr	81	52	43	206	227	244	232	116	78	227
ppm	Zr	45	37	27	32	28	34	44	62	45	106
mol. %	Mg#	80.8	83.2	84.4	78.5	74.8	67.1	62.1	76.7	78.7	55.7
n/a	Cr/V	25.4	41.9	46.9	25.5	4.5	3.6	1.3	17.4	24.2	1.1
n/a	Ni/Cu	17.1	25.5	27.6	1.19	0.89	3.97	2.09	3.79	2.81	0.50

Table 3

Sample:	IT-3	IT-4	IT-5	IT-8	IT-14	IT-16	IT-18	IT-19	IT-21	IT-22	IT-23	IT-26	IT-29
Height (m):	3.0	34.4	43.8	115.6	210.9	285.9	331.3	400.0	440.6	467.2	475.0	548.4	621.9
Rock:	BOG	BOG	BOG	BOG	LU	LU	LU	LU	LU	COG	CG	CG	CG
Rb	7.95	6.9	6.73	5.92	6.13	2.59	2.95	2.17	3.08	6.32	5.84	5.51	6.01
Ba	68.8	61.7	52.4	39.8	31.5	25.2	33.8	24.3	36.3	57.7	57.8	61.4	69.4
Sr	68.2	60.4	57	40.8	32.1	36.5	36.5	33	39.1	193	234	218	244
Y	8.45	7	6.77	5.39	3.56	3.76	3.37	3.72	4.59	4.93	4.83	7.75	7.54
Zr	43.1	30.2	30.1	24.5	12.5	15.6	11.3	11.5	15	23.4	10.4	20.9	22.6
Hf	1.08	0.74	0.77	0.62	0.33	0.39	0.29	0.29	0.4	0.55	0.3	0.58	0.58
Nb	2.79	2.15	2.17	1.41	0.95	1.06	0.86	0.81	1.1	1.71	1.3	1.43	1.49
Ta	0.32	0.25	0.22	0.21	0.15	0.15	0.15	0.14	0.28	0.31	0.25	0.24	0.25
Th	0.93	0.79	0.78	0.66	0.56	0.38	0.33	0.31	0.31	0.58	0.42	0.43	0.65
Pb	2.05	1.75	1.39	1.31	0.71	0.54	0.79	0.86	1.84	1.57	1.44	1.19	2.46
La	4.86	4.00	4.04	3.48	2.18	2.12	1.93	1.75	2.03	3.10	2.83	2.89	3.05
Ce	9.96	8.44	8.77	7.52	4.78	4.49	4.21	3.80	4.46	6.65	5.89	6.35	6.81
Nd	5.35	4.51	4.52	3.96	2.50	2.31	2.23	2.07	2.58	3.51	3.12	3.85	3.97
Sm	1.27	1.06	1.02	0.87	0.55	0.52	0.51	0.51	0.63	0.81	0.75	1.01	1.03
Eu	0.38	0.32	0.30	0.22	0.17	0.17	0.15	0.16	0.21	0.39	0.49	0.49	0.58
Gd	1.49	1.27	1.21	0.98	0.66	0.63	0.61	0.60	0.75	0.89	0.81	1.26	1.22
Tb	0.24	0.20	0.20	0.16	0.10	0.10	0.10	0.10	0.13	0.14	0.13	0.22	0.20
Dy	1.63	1.37	1.26	1.01	0.67	0.68	0.65	0.67	0.84	0.90	0.87	1.41	1.39
Ho	0.32	0.28	0.27	0.22	0.14	0.14	0.13	0.15	0.18	0.19	0.18	0.30	0.29
Er	0.95	0.80	0.74	0.60	0.40	0.43	0.36	0.44	0.50	0.51	0.54	0.86	0.82
Tm	0.13	0.12	0.11	0.09	0.06	0.06	0.06	0.06	0.08	0.08	0.08	0.13	0.12
Yb	0.91	0.75	0.75	0.58	0.41	0.43	0.38	0.47	0.50	0.50	0.51	0.81	0.79
Lu	0.14	0.11	0.11	0.09	0.06	0.07	0.06	0.07	0.08	0.08	0.08	0.12	0.12
Th/Yb_N	5.67	5.84	5.77	6.31	7.58	4.9	4.82	3.66	3.44	6.43	4.57	2.94	4.56
Nb/Nb*	0.45	0.42	0.42	0.32	0.3	0.41	0.37	0.38	0.48	0.44	0.41	0.44	0.37
Eu/Eu*	0.84	0.84	0.82	0.73	0.86	0.91	0.82	0.88	0.93	1.40	1.92	1.33	1.58
La/Sm_N	2.40	2.36	2.48	2.51	2.48	2.55	2.37	2.15	2.02	2.40	2.36	1.79	1.86
Gd/Yb_N	1.33	1.37	1.31	1.37	1.30	1.19	1.30	1.03	1.22	1.44	1.29	1.26	1.25
ΣREE	27.6	23.2	23.3	19.8	12.7	12.2	11.4	10.9	13.0	17.7	16.3	19.7	20.4

[1]Calculations have been normalised to primitive mantle (McDonough & Sun 1995). $Eu/Eu^* = Eu_N/(Sm_N \times Gd_N)^{0.5}$, $Nb/Nb^* = Nb_N/(Th_N \times La_N)^{0.5}$

Table 4

Composition:		QU1-1-9 dolerite[1]	Uncontaminated QU1-1-9 dolerite[2]	Unevolved QU1-1-9 dolerite[3]	Contaminated QU1-1-9 dolerite[4]	Proterozoic Basement[5]	Ecca country rocks[6]
wt.%	SiO_2	52.2	49.8	49.3	52.4	69.3	64.6
wt.%	TiO_2	0.86	0.86	0.79	0.86	0.76	0.58
wt.%	Al_2O_3	15.2	15.2	13.9	15.3	13.6	19.5
wt.%	Fe_2O_{3t}	11.2	11.6	12.0	10.8	5.37	5.95
wt.%	MnO	0.16	0.17	0.17	0.16	0.11	0.08
wt.%	MgO	7.76	8.44	12.11	7.03	0.79	2.71
wt.%	CaO	10.6	11.4	10.5	10.2	2.57	0.96
wt.%	Na_2O	2.19	2.10	1.92	2.24	2.79	1.60
wt.%	K_2O	0.51	0.06	0.06	0.74	4.45	3.26
wt.%	P_2O_5	0.12	0.10	0.09	0.13	0.28	0.22
wt.%	H_2O	0.50	0.50	0.50	0.96	0.50	0.50
ppm	S	200	167	150	219	500	500
ppm	Sc	36	38	34	35	16	17
ppm	V	234	253	228	226	63	85
ppm	Cr	452	489	472	308	117	87
ppm	Co	33	36	127	32	8.2	11.1
ppm	Ni	86	94	334	69	13	70
ppm	Cu	80	86	77	78	28	35
ppm	Zn	85	85	76	86	88	91
ppm	Rb	20.5	1.02	0.92	31.9	215	161
ppm	Ba	135	44.8	40.3	183	947	553
ppm	Sr	188	150	135	210	533	246
ppm	Y	22.9	19.5	17.6	24.1	39.3	47.0
ppm	Zr	80.0	50.8	45.8	96	342	192
ppm	Hf	2.12	1.30	1.17	2.57	9.54	5.35
ppm	Nb	6.01	4.40	3.96	6.30	10.0	15.0
ppm	Th	1.25	2.22	2.00	2.01	14.3	19.7
ppm	La	8.44	1.23	1.11	12.2	73.3	51.3
ppm	Ce	18.1	2.56	2.30	26.2	158	103
ppm	Nd	9.75	3.01	2.71	13.3	70.4	49.4
ppm	Sm	2.80	1.62	1.46	3.44	13.4	10.5
ppm	Eu	0.98	0.87	0.79	1.04	1.93	1.57
ppm	Gd	2.81	1.90	1.71	3.31	11.0	8.1
ppm	Tb	0.58	0.46	0.42	0.65	1.65	1.41
ppm	Dy	3.41	2.69	2.42	3.82	9.91	6.71
ppm	Ho	0.71	0.57	0.51	0.79	1.98	1.37
ppm	Er	1.95	1.54	1.38	2.18	5.67	8.07
ppm	Tm	0.27	0.21	0.19	0.30	0.82	1.41
ppm	Yb	2.13	1.75	1.58	2.35	5.54	6.71
ppm	Lu	0.32	0.27	0.24	0.35	0.79	1.37
$^{87}Sr/^{86}Sr_{(i)}$		0.70566	0.70449	0.70449	0.70709	0.71580	0.71232

[1]Whole-rock composition from sample QU1-1-9 and Sr-isotopic composition from sample QU1-1-4 of Neumann *et al.* (2011).

[2]Sample QU1-1-9 minus 10 g of Namaqua-Natal basement rock (Bailie *et al.* 2017) using the method of Mungall *et al.* (2010).

[3]Uncontaminated QU1-1-9 dolerite plus 10% olivine using PRIMELT (Herzberg and Asimow 2015).

[4]QU1-1-9 dolerite composition after batch-assimilation of 6 g of Namaqua-Natal basement rock at 1 kbar.

[5]Average Namaqua-Natal basement rock composition from Bailie *et al.* (2017) with Sr-isotope composition from sample Kan1.

[6]Average composition of Ecca Group metasedimentary country rocks (Neumann *et al.* 2011) with the Sr-isotope composition of Ecca Group hornfels (Lightfoot and Naldrett 1984)

Table 5

	Lobe:	**Ingeli**									**Horseshoe**		
	Unit:	Basal olivine gabbronorite			Lherzolite unit			Central gabbronorite			Olivine gabbronorite		
	Type:	x̄	2σ	model	x̄	2σ	model	x̄	2σ	model	x̄	2σ	model
	Model liquid:	Contaminated QU1-1-9 dolerite			Contaminated QU1-1-9 dolerite			QU1-1-9 Karoo dolerite			Contaminated QU1-1-9 dolerite		
	Model T (°C):			1156			1154			1124			1154
	liquid:cumulate			32:68			17:83			14:86			44:56
wt.%	SiO_2	42.1	3.96	43.7	41.5	1.01	40.8	50.9	0.79	50.6	45.0	2.98	44.6
wt.%	TiO_2	0.22	0.32	0.28	0.18	0.06	0.19	0.28	0.11	0.336	0.42	0.17	0.41
wt.%	Al_2O_3	5.00	1.45	4.95	3.11	0.29	2.99	18.9	5.40	16.6	6.53	2.39	7.01
wt.%	Fe_2O_{3t}	14.9	1.07	15.6	15.4	2.35	17.5	6.58	2.82	8.46	15.0	1.91	15.3
wt.%	MgO	33.4	3.77	31.8	37.3	2.25	36.6	8.66	0.79	*10.1*	27.7	5.78	27.0
wt.%	CaO	3.66	1.97	3.59	2.16	0.32	2.08	12.5	2.26	12.5	4.31	1.60	4.74
wt.%	Na_2O	0.18	0.55	0.73	*bdl*	*bdl*	0.38	1.72	0.56	1.57	0.44	0.49	0.99
ppm	Ba	55.7	25.1	59.2	30.2	10.6	31.3	62.9	11.9	51.3	*nd*	*nd*	*nd*
ppm	Sr	56.6	23.1	67.9	35.4	5.72	35.8	232	26.2	*190*	90.1	30.2	67.3
ppm	Y	6.90	2.51	7.88	3.80	0.94	4.21	6.71	3.26	6.85	*nd*	*nd*	*nd*
ppm	Zr	32.0	15.8	31.6	13.2	4.00	17.1	18.0	13.2	20.7	50.6	12.5	*31.5*
ppm	Hf	0.80	0.39	0.83	0.34	0.11	0.44	0.49	0.32	0.63	*nd*	*nd*	*nd*
ppm	Nb	2.13	1.13	2.06	0.96	0.25	1.10	1.41	0.19	1.34	*nd*	*nd*	*nd*
ppm	Th	0.79	0.22	0.65	0.38	0.21	0.34	0.50	0.26	0.30	*nd*	*nd*	*nd*
ppm	La	4.10	1.14	3.97	2.00	0.34	2.10	2.92	0.23	3.11	*nd*	*nd*	*nd*
ppm	Ce	8.67	2.02	8.50	4.35	0.73	4.49	6.37	0.92	6.31	*nd*	*nd*	*nd*
ppm	Nd	4.59	1.12	4.32	2.34	0.42	2.29	3.65	0.92	3.49	*nd*	*nd*	*nd*
ppm	Sm	1.06	0.33	1.12	0.54	0.10	0.59	0.93	0.31	1.01	*nd*	*nd*	*nd*
ppm	Eu	0.31	0.13	0.34	0.17	0.04	0.18	0.52	0.10	0.63	*nd*	*nd*	*nd*
ppm	Gd	1.24	0.42	1.07	0.65	0.12	0.57	1.10	0.50	0.99	*nd*	*nd*	*nd*
ppm	Tb	0.20	0.07	0.21	0.10	0.00	0.11	0.17	0.13	0.21	*nd*	*nd*	*nd*
ppm	Dy	1.32	0.51	1.24	0.70	0.16	0.66	1.22	0.61	1.22	*nd*	*nd*	*nd*
ppm	Ho	0.27	0.08	0.26	0.15	0.04	0.14	0.26	0.13	0.25	*nd*	*nd*	*nd*
ppm	Er	0.77	0.29	0.71	0.43	0.10	0.38	0.74	0.35	0.67	*nd*	*nd*	*nd*
ppm	Tm	0.11	0.03	0.10	0.06	0.02	0.05	0.11	0.03	0.09	*nd*	*nd*	*nd*
ppm	Yb	0.75	0.27	0.76	0.44	0.11	0.40	0.70	0.34	0.72	*nd*	*nd*	*nd*
ppm	Lu	0.11	0.04	0.11	0.07	0.01	0.06	0.11	0.04	0.11	*nd*	*nd*	*nd*

[1]*Italicized* numbers are modelled concentrations outside of the measured range.

Table 6

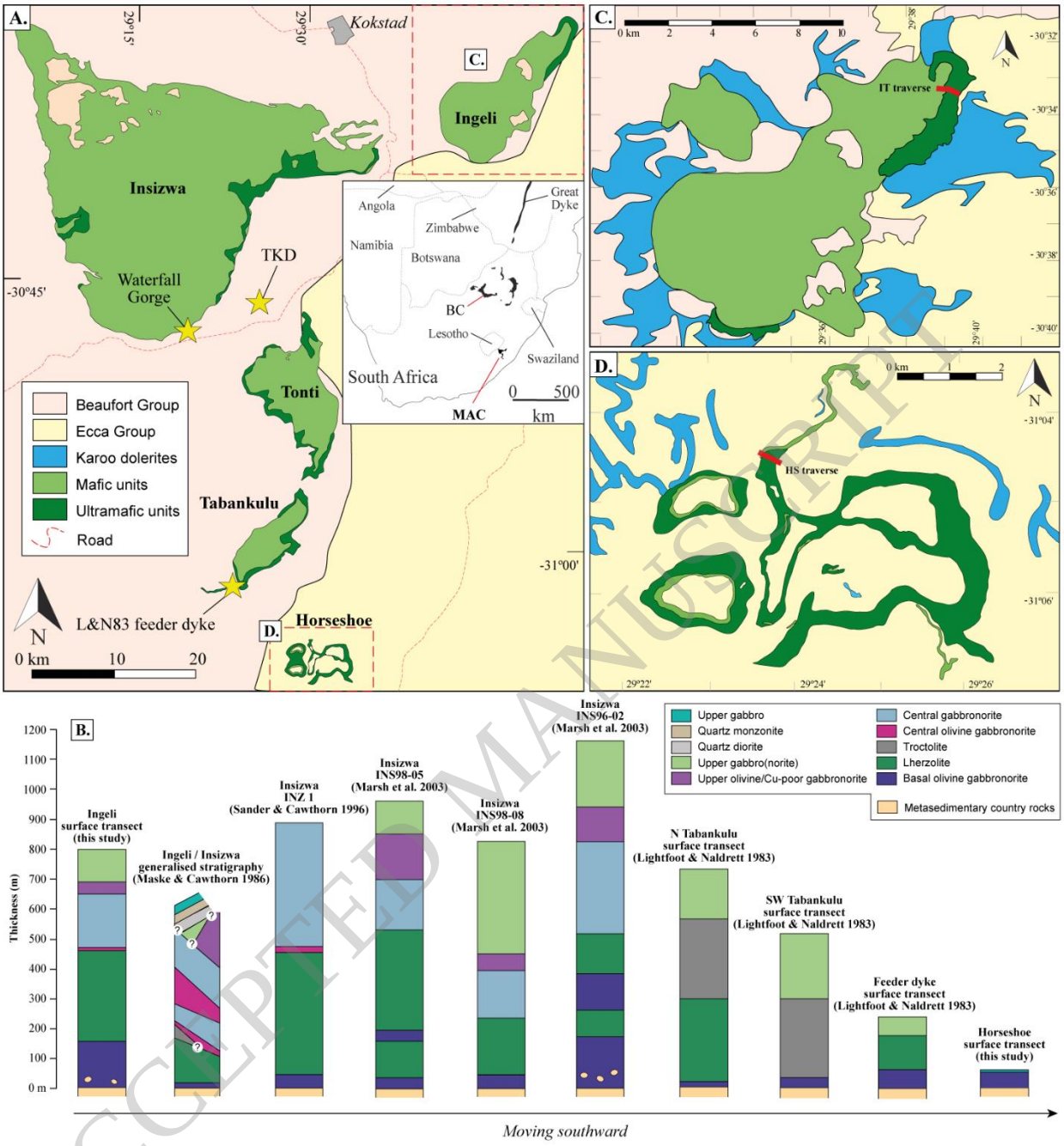

Figure 1

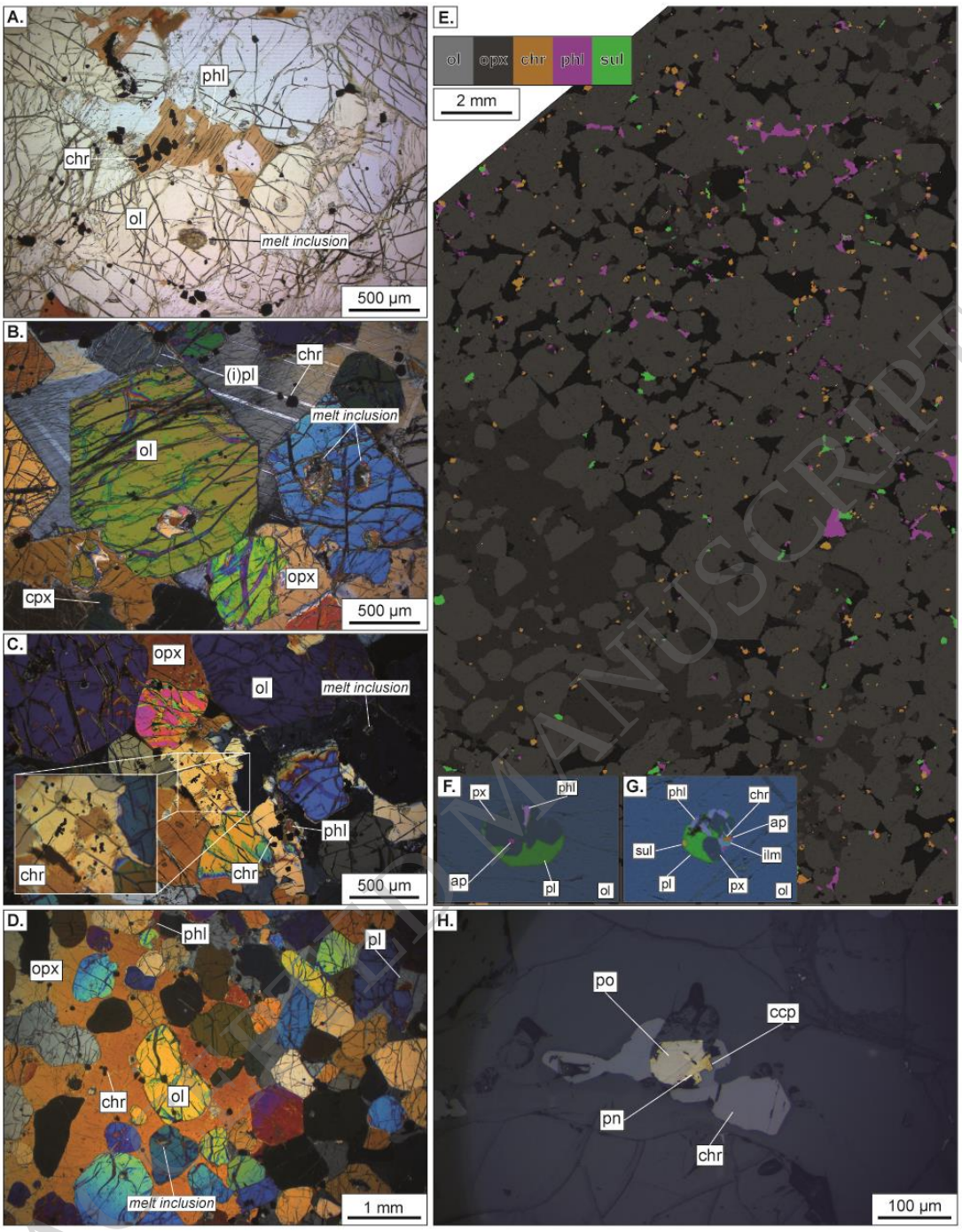

Figure 2

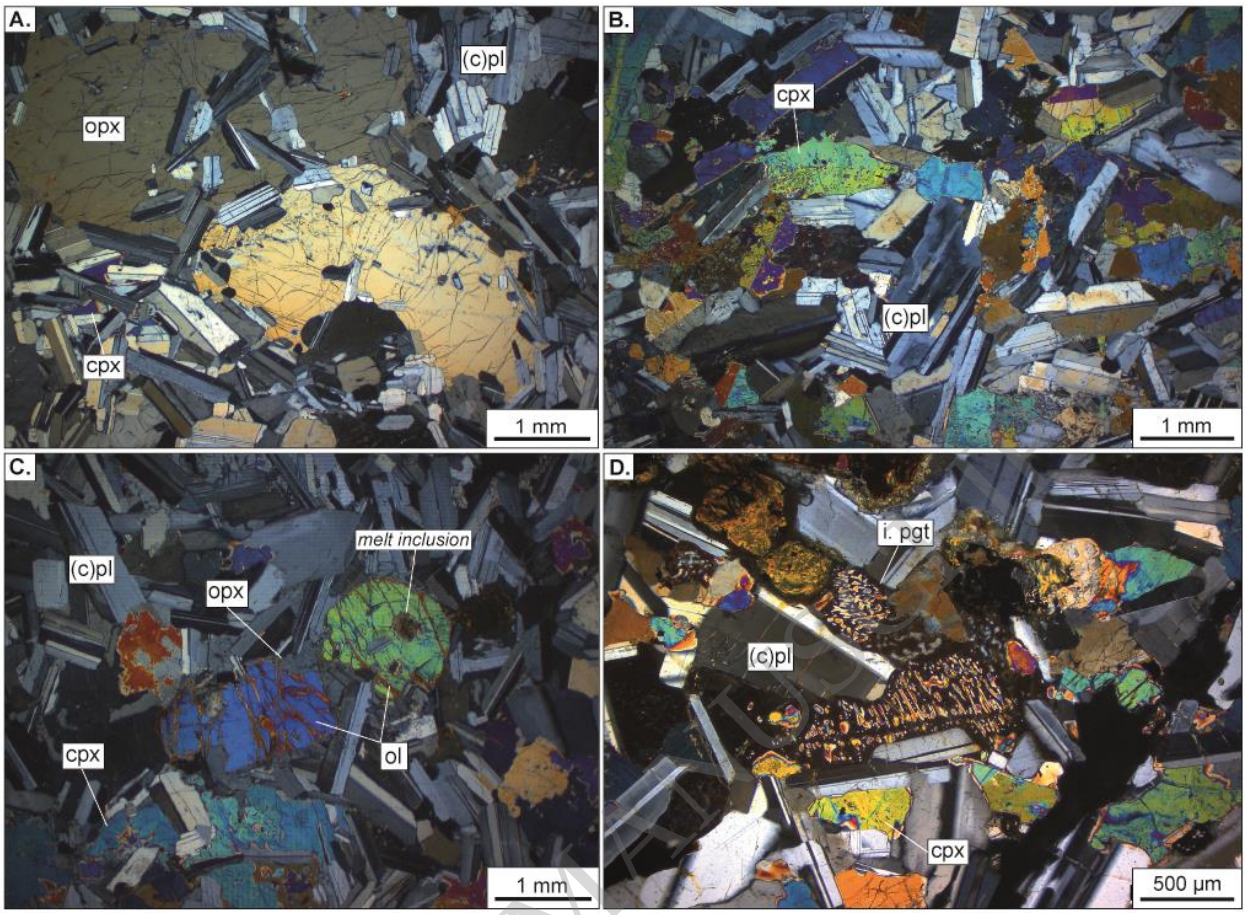

Figure 3

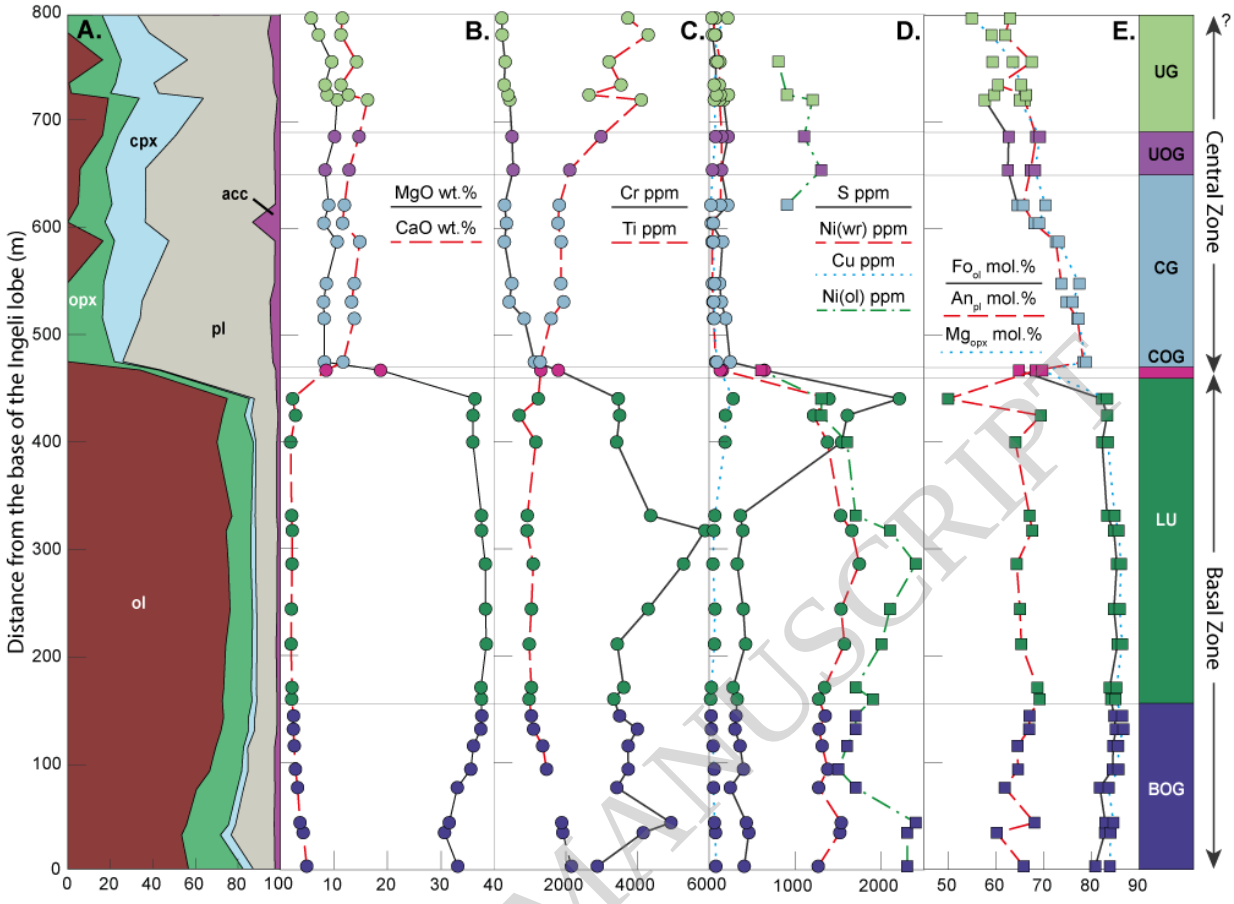

Figure 4

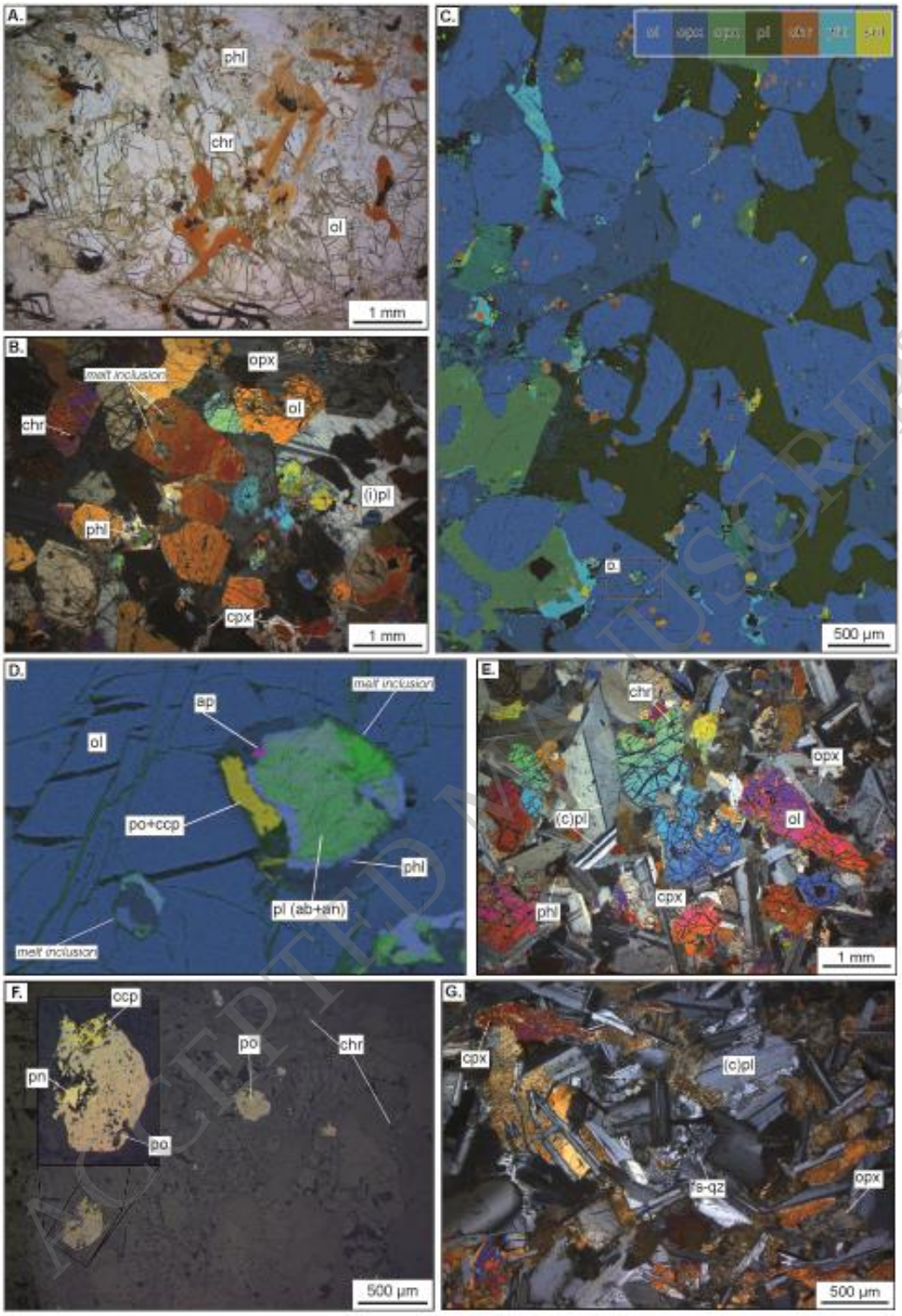

Figure 5

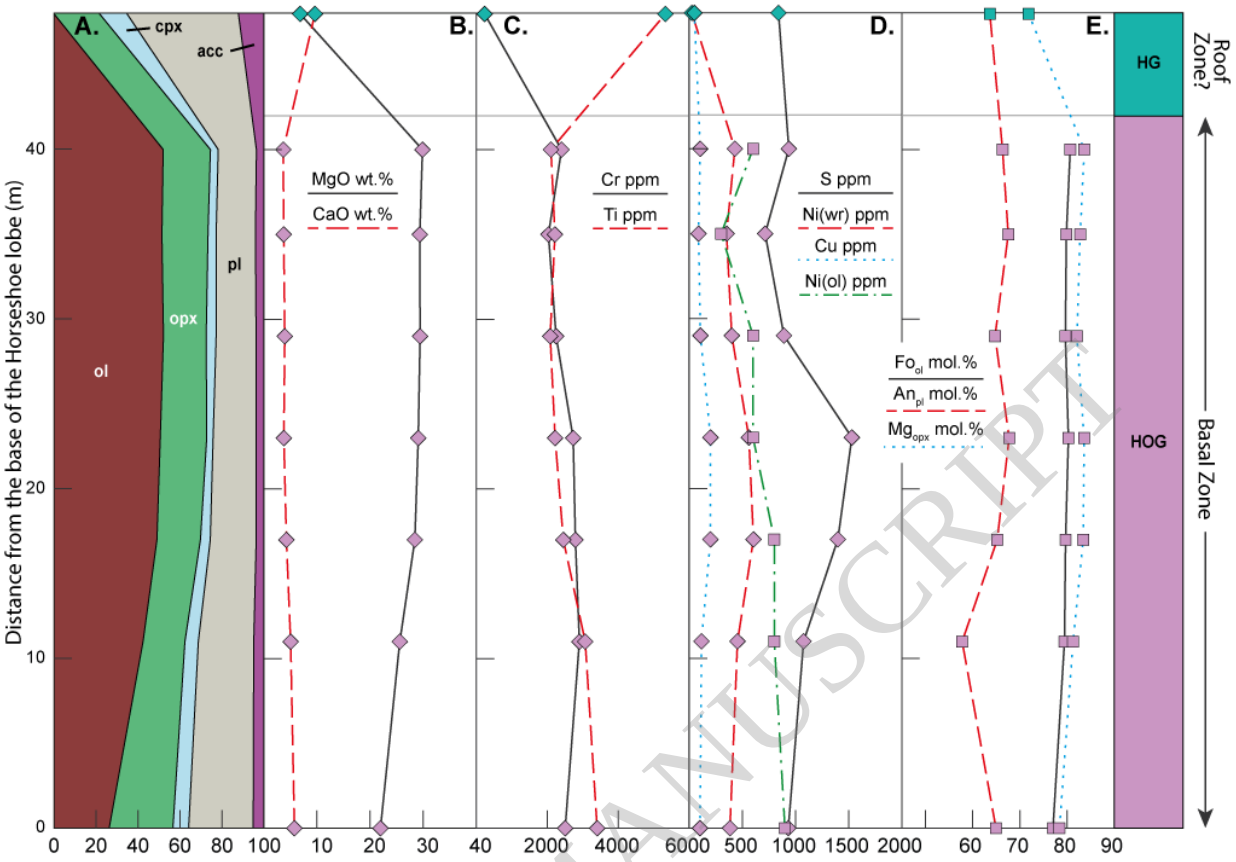

Figure 6

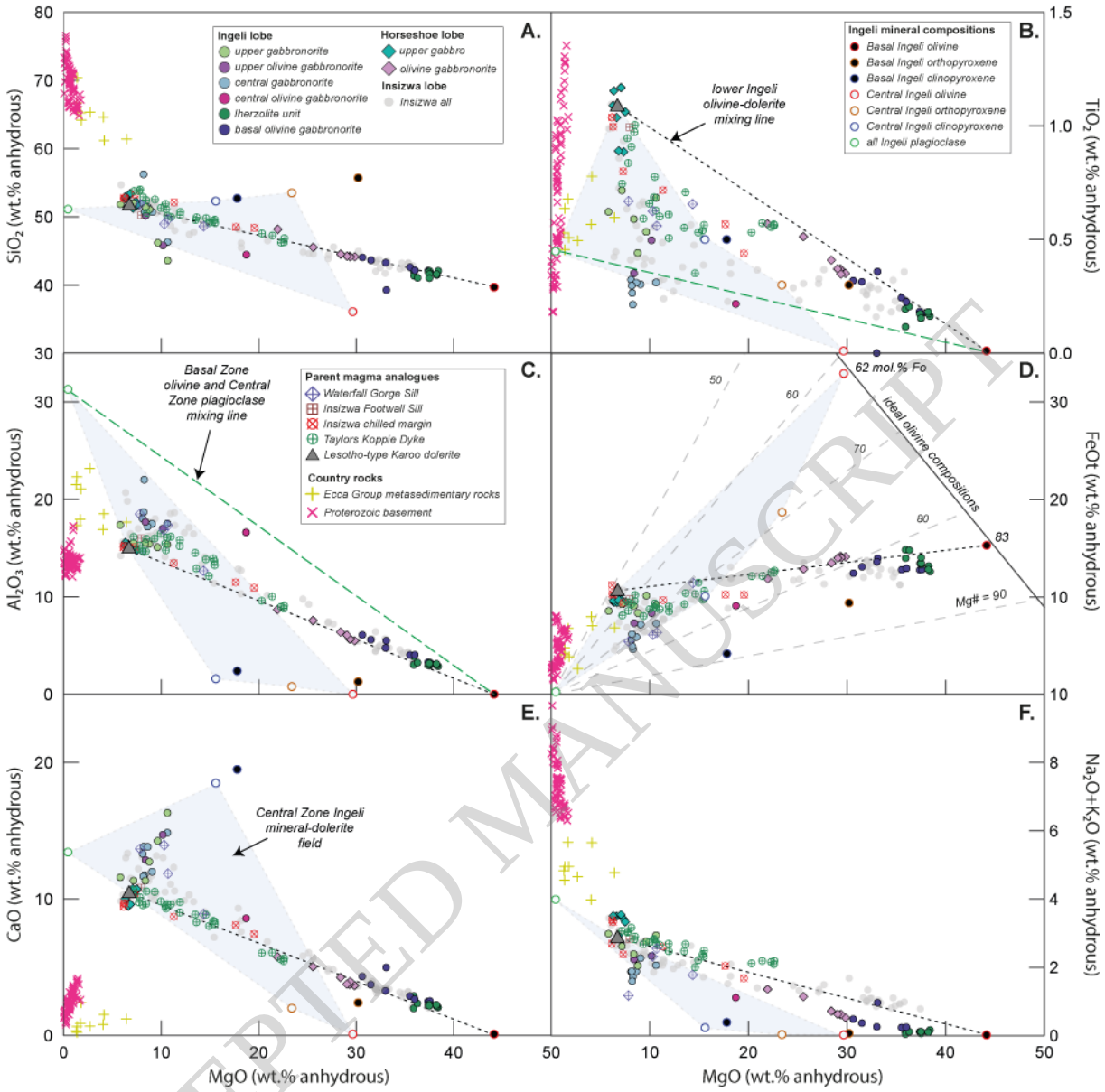

Figure 7

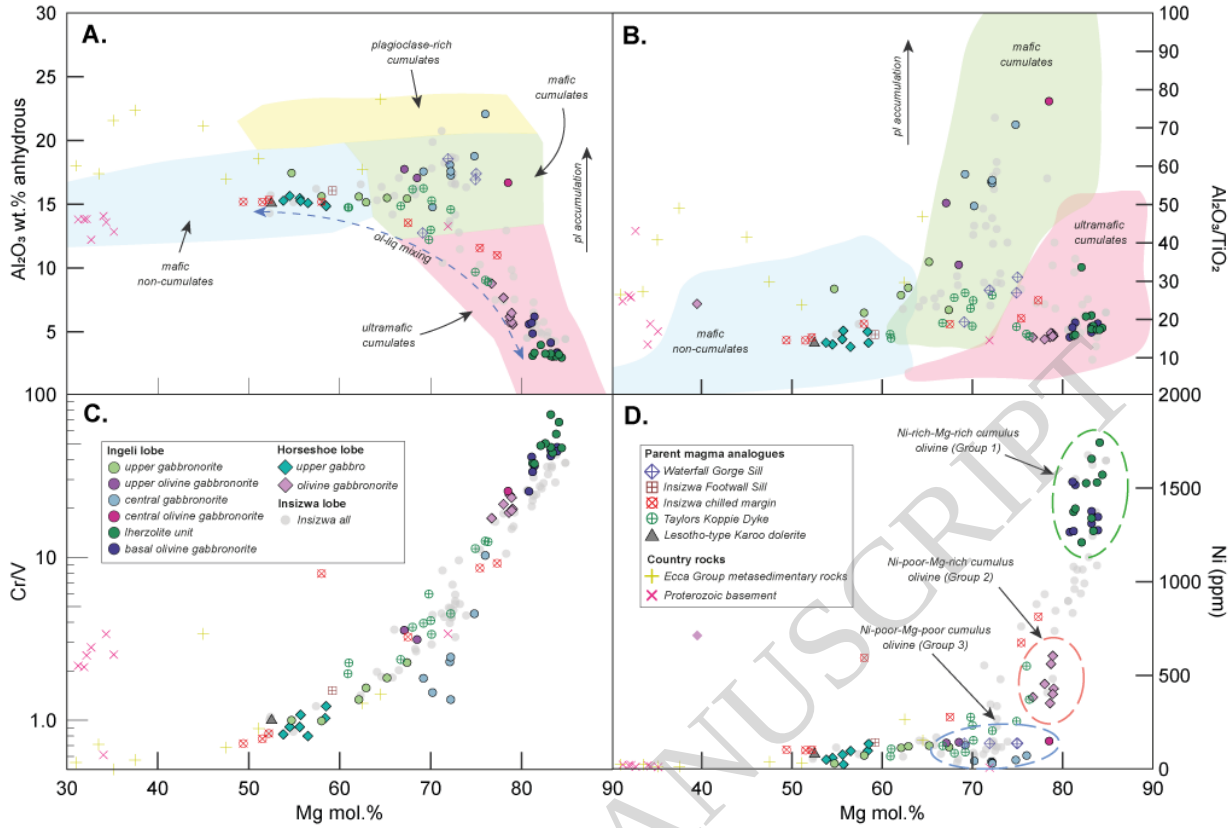

Figure 8

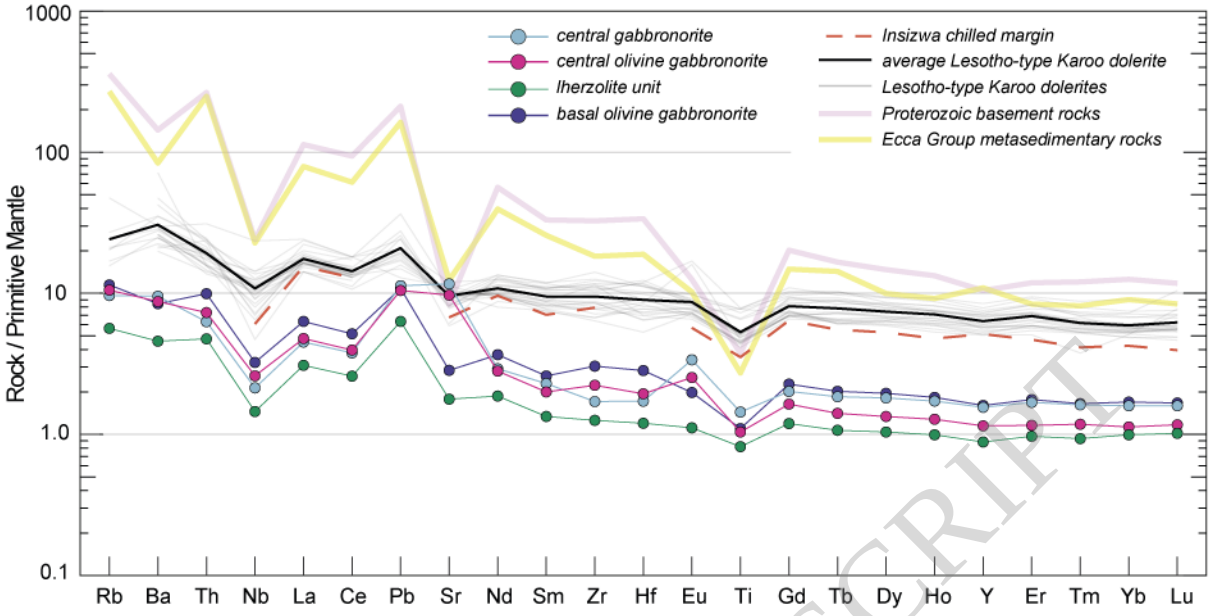

Figure 9

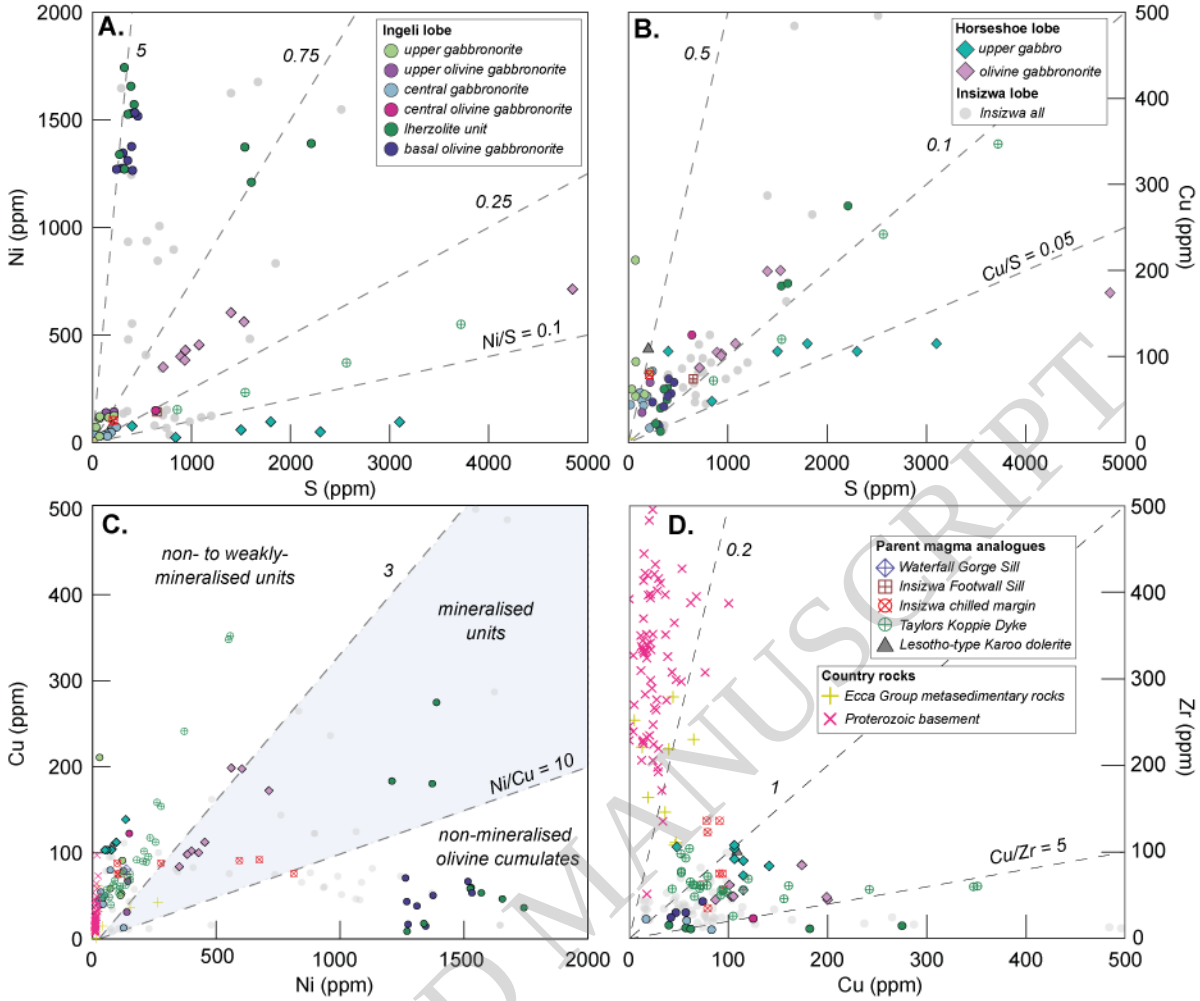

Figure 10

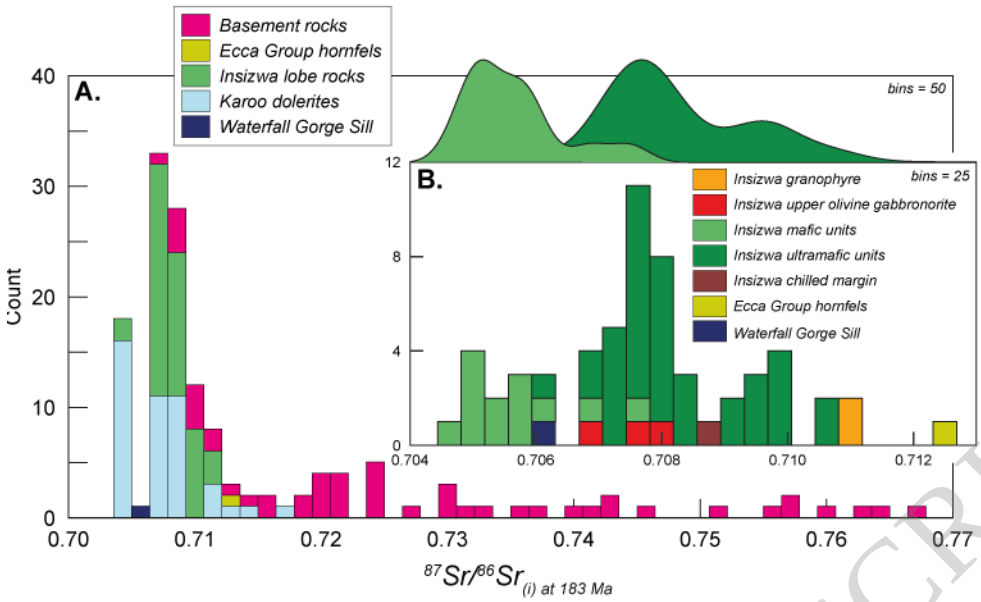

Figure 11

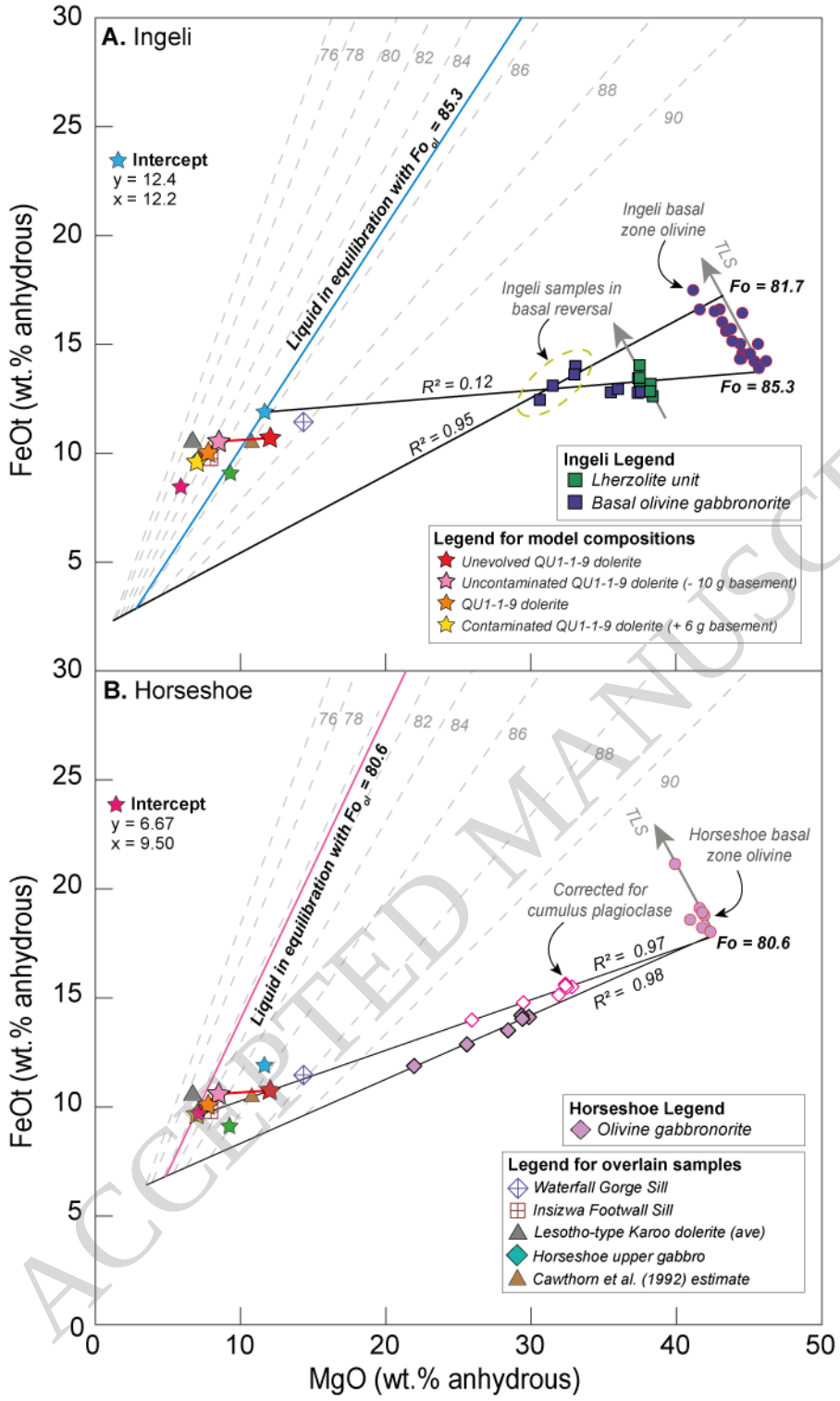

Figure 12

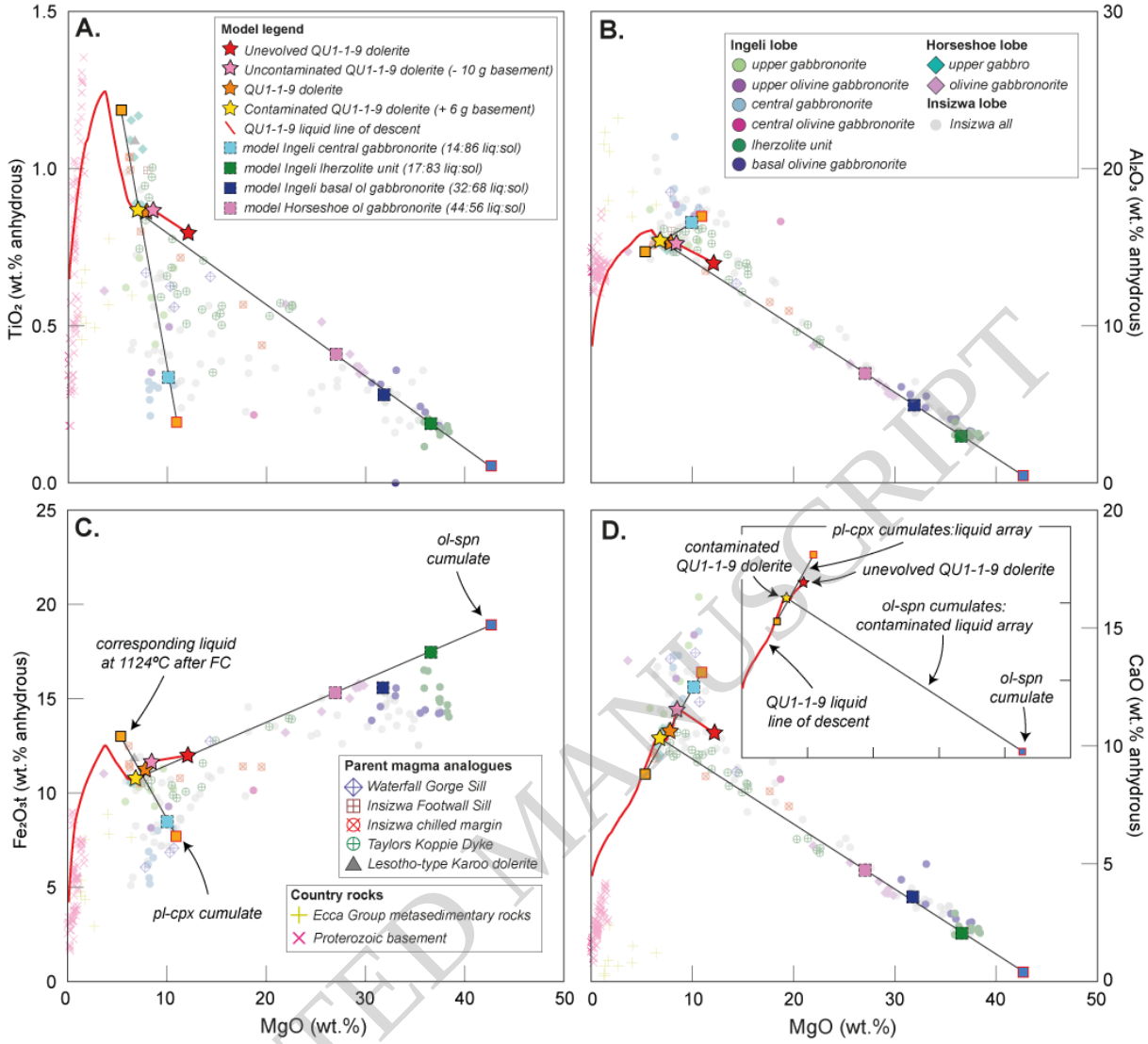

Figure 13

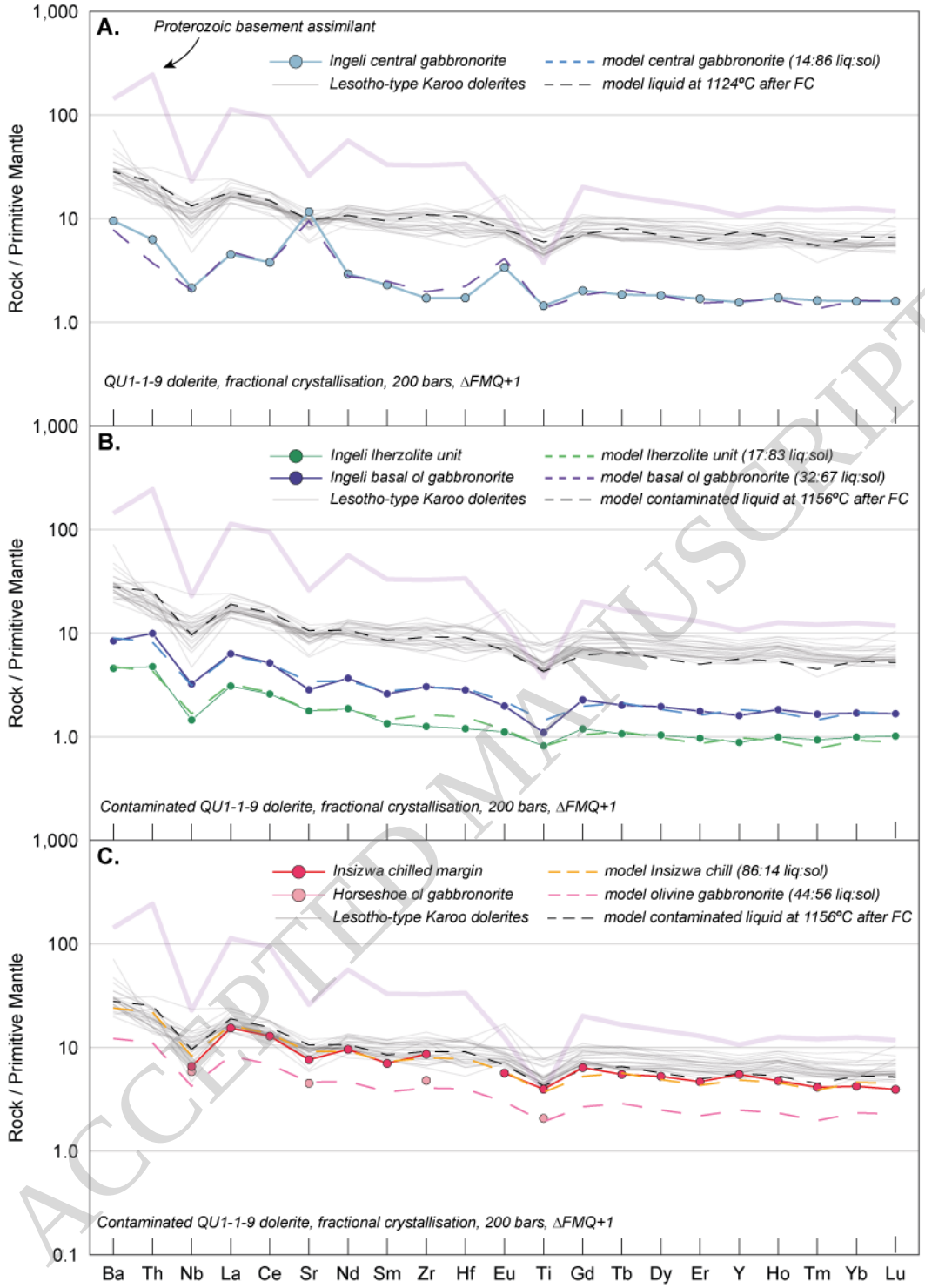

Figure 14

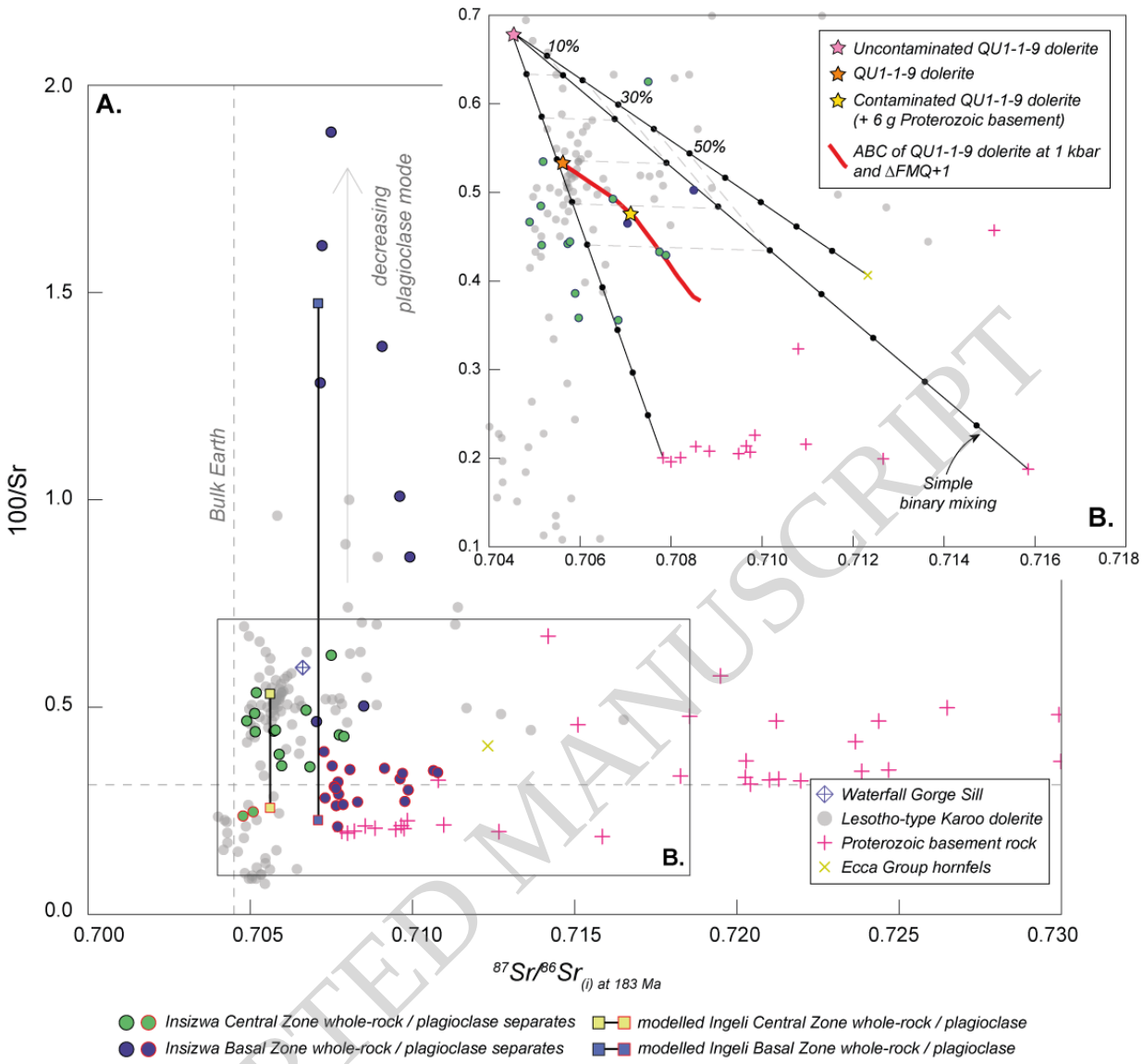

Figure 15

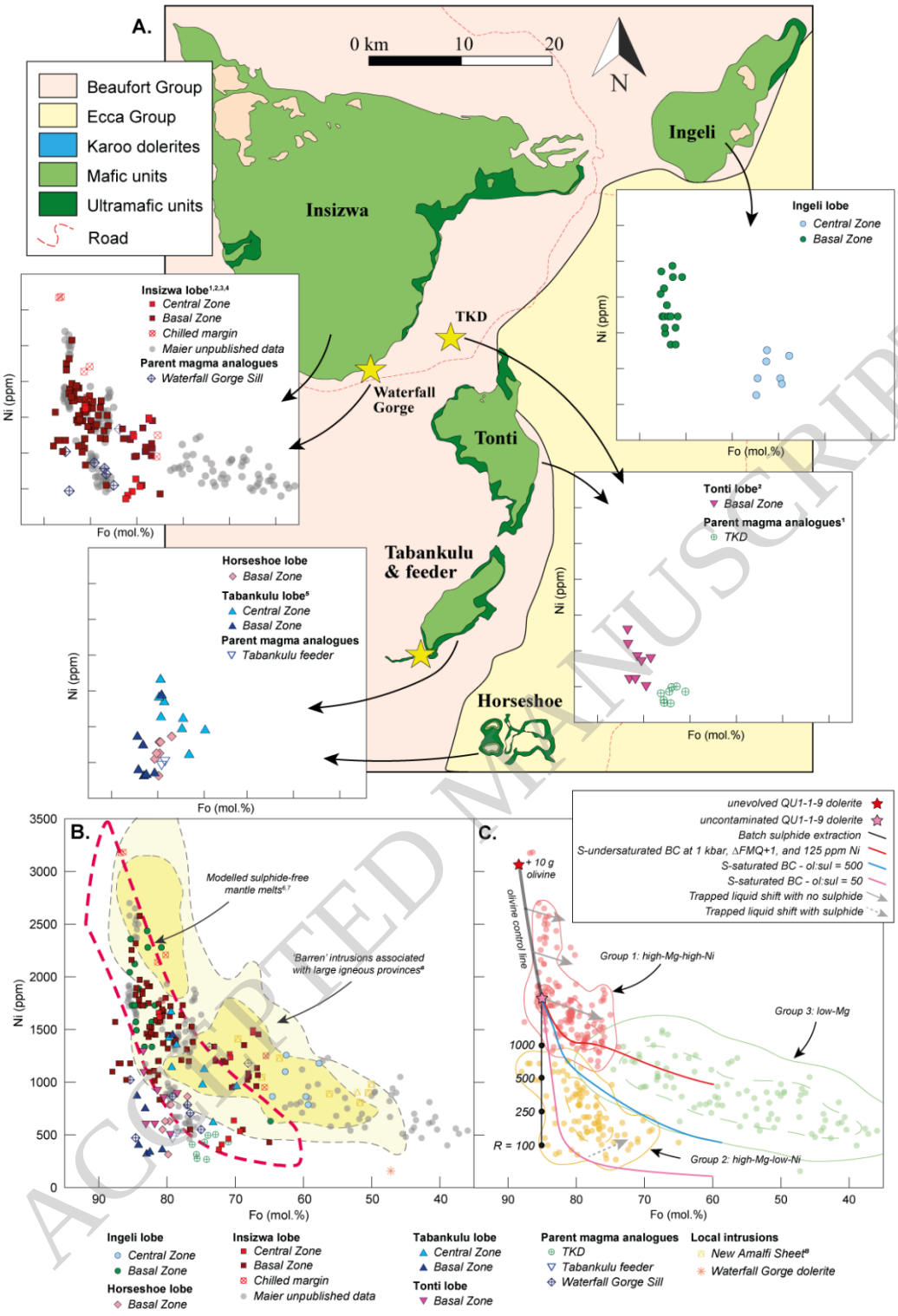

Figure 16

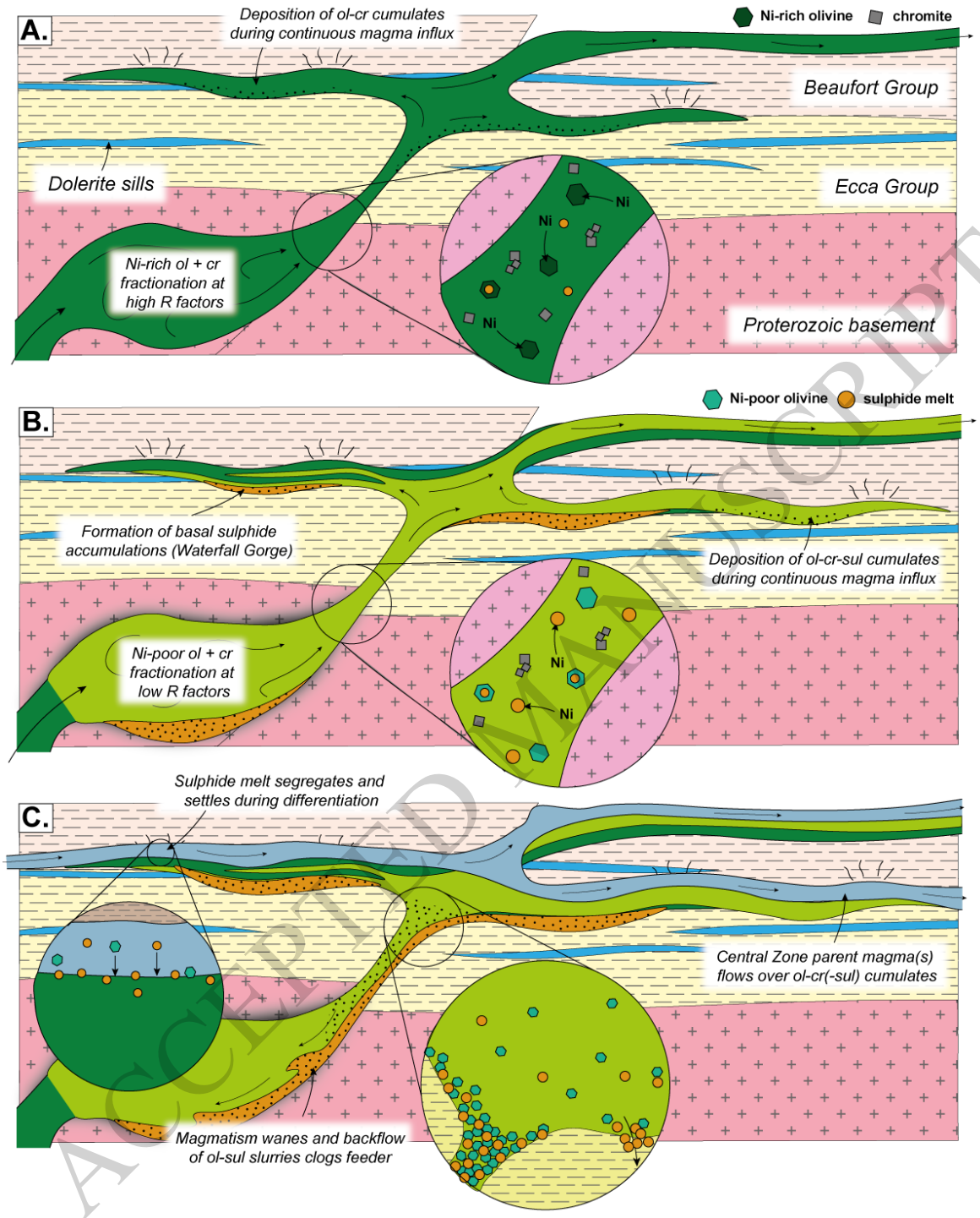

Figure 17